

See discussions, stats, and author profiles for this publication at: <https://www.researchgate.net/publication/221690810>

Insight into the Dinuclear $\{\text{Fe}(\text{NO})(2)\}_2\{\text{Fe}(\text{NO})(2)\}_2$ and Mononuclear $\{\text{Fe}(\text{NO})(2)\}_2$ Dinitrosyliron Complexes

ARTICLE in INORGANIC CHEMISTRY · MARCH 2012

Impact Factor: 4.76 · DOI: 10.1021/ic202332d · Source: PubMed

CITATIONS

21

READS

25

8 AUTHORS, INCLUDING:



I-Jui Hsu

National Taipei University of Technology

51 PUBLICATIONS 484 CITATIONS

SEE PROFILE



Chien-Hong Chen

Chung Shan Medical University

23 PUBLICATIONS 376 CITATIONS

SEE PROFILE



Ling-Yun Jang

National Synchrotron Radiation Research Cen...

140 PUBLICATIONS 1,610 CITATIONS

SEE PROFILE

Insight into the Dinuclear $\{\text{Fe}(\text{NO})_2\}^{10}\{\text{Fe}(\text{NO})_2\}^{10}$ and Mononuclear $\{\text{Fe}(\text{NO})_2\}^{10}$ Dinitrosyliron Complexes

Shih-Wey Yeh,[†] Chih-Wei Lin,[†] Ya-Wen Li,[‡] I-Jui Hsu,^{*,‡} Chien-Hong Chen,[§] Ling-Yun Jang,[¶] Jyh-Fu Lee,[¶] and Wen-Feng Liaw^{*,†}

[†]Department of Chemistry and Frontier Research Center of Fundamental and Applied Science of Matters, National Tsing Hua University, Hsinchu 30013, Taiwan

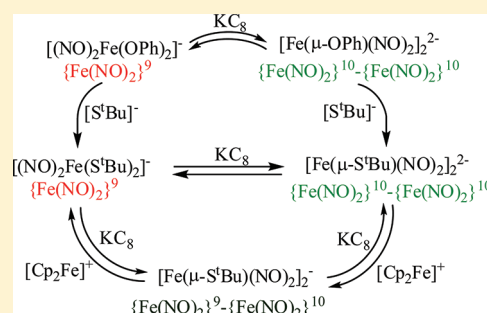
[‡]Department of Molecular Science and Engineering, National Taipei University of Technology, Taipei 10608, Taiwan

[§]School of Applied Chemistry, Chung Shan Medical University, Taichung City 40201, Taiwan

[¶]National Synchrotron Radiation Research Center (NSRRC), Hsinchu 30076, Taiwan

S Supporting Information

ABSTRACT: The reversible redox transformations $[(\text{NO})_2\text{Fe}(\text{S}^t\text{Bu})_2]^- \rightleftharpoons [\text{Fe}(\mu\text{-S}^t\text{Bu})(\text{NO})_2]_2^{2-} \rightleftharpoons [\text{Fe}(\mu\text{-S}^t\text{Bu})(\text{NO})_2]_2^- \rightleftharpoons [\text{Fe}(\mu\text{-S}^t\text{Bu})(\text{NO})_2]_2$ and $[\text{cation}][(\text{NO})_2\text{Fe}(\text{SEt})_2] \rightleftharpoons [\text{cation}]_2[(\text{NO})_2\text{Fe}(\text{SEt})_2]$ (cation = K^+ -18-crown-6 ether) are demonstrated. The counteraction of the $\{\text{Fe}(\text{NO})_2\}^9$ dinitrosyliron complexes (DNICs) functions to control the formation of the $\{\text{Fe}(\text{NO})_2\}^{10}\{\text{Fe}(\text{NO})_2\}^{10}$ dianionic reduced Roussin's red ester (RRE) $[\text{PPN}]_2[\text{Fe}(\mu\text{-SR})(\text{NO})_2]_2$ or the $\{\text{Fe}(\text{NO})_2\}^{10}$ dianionic reduced monomeric DNIC $[\text{K}^+\text{-18-crown-6 ether}]_2[(\text{NO})_2\text{Fe}(\text{SR})_2]$ upon reduction of the $\{\text{Fe}(\text{NO})_2\}^9$ DNICs $[\text{cation}][(\text{NO})_2\text{Fe}(\text{SR})_2]$ (cation = PPN^+ , K^+ -18-crown-6 ether; R = alkyl). The binding preference of ligands $[\text{OPh}]^-/[\text{SR}]^-$ toward the $\{\text{Fe}(\text{NO})_2\}^{10}\{\text{Fe}(\text{NO})_2\}^{10}$ motif of dianionic reduced RRE follows the ligand-displacement series $[\text{SR}]^- > [\text{OPh}]^-$. Compared to the Fe K-edge preedge energy falling within the range of 7113.6–7113.8 eV for the dinuclear $\{\text{Fe}(\text{NO})_2\}^9\{\text{Fe}(\text{NO})_2\}^9$ DNICs and 7113.4–7113.8 eV for the mononuclear $\{\text{Fe}(\text{NO})_2\}^9$ DNICs, the $\{\text{Fe}(\text{NO})_2\}^{10}$ dianionic reduced monomeric DNICs and the $\{\text{Fe}(\text{NO})_2\}^{10}\{\text{Fe}(\text{NO})_2\}^{10}$ dianionic reduced RREs containing S/O/N-ligation modes display the characteristic preedge energy 7113.1–7113.3 eV, which may be adopted to probe the formation of the EPR-silent $\{\text{Fe}(\text{NO})_2\}^{10}\{\text{Fe}(\text{NO})_2\}^{10}$ dianionic reduced RREs and $\{\text{Fe}(\text{NO})_2\}^{10}$ dianionic reduced monomeric DNICs in biology. In addition to the characteristic Fe/S K-edge preedge energy, the IR ν_{NO} spectra may also be adopted to characterize and discriminate $[(\text{NO})_2\text{Fe}(\mu\text{-S}^t\text{Bu})_2]^-$ [IR ν_{NO} 1809 vw, 1778 s, 1753 cm^{-1} (KBr)], $[\text{Fe}(\mu\text{-S}^t\text{Bu})(\text{NO})_2]_2^{2-}$ [IR ν_{NO} 1674 s, 1651 cm^{-1} (KBr)], $[\text{Fe}(\mu\text{-S}^t\text{Bu})(\text{NO})_2]_2^-$ [IR ν_{NO} 1637 m, 1613 s, 1578 s, 1567 cm^{-1} (KBr)], and $[\text{K-18-crown-6 ether}]_2[(\text{NO})_2\text{Fe}(\text{SEt})_2]$ [IR ν_{NO} 1604 s, 1560 cm^{-1} (KBr)].



INTRODUCTION

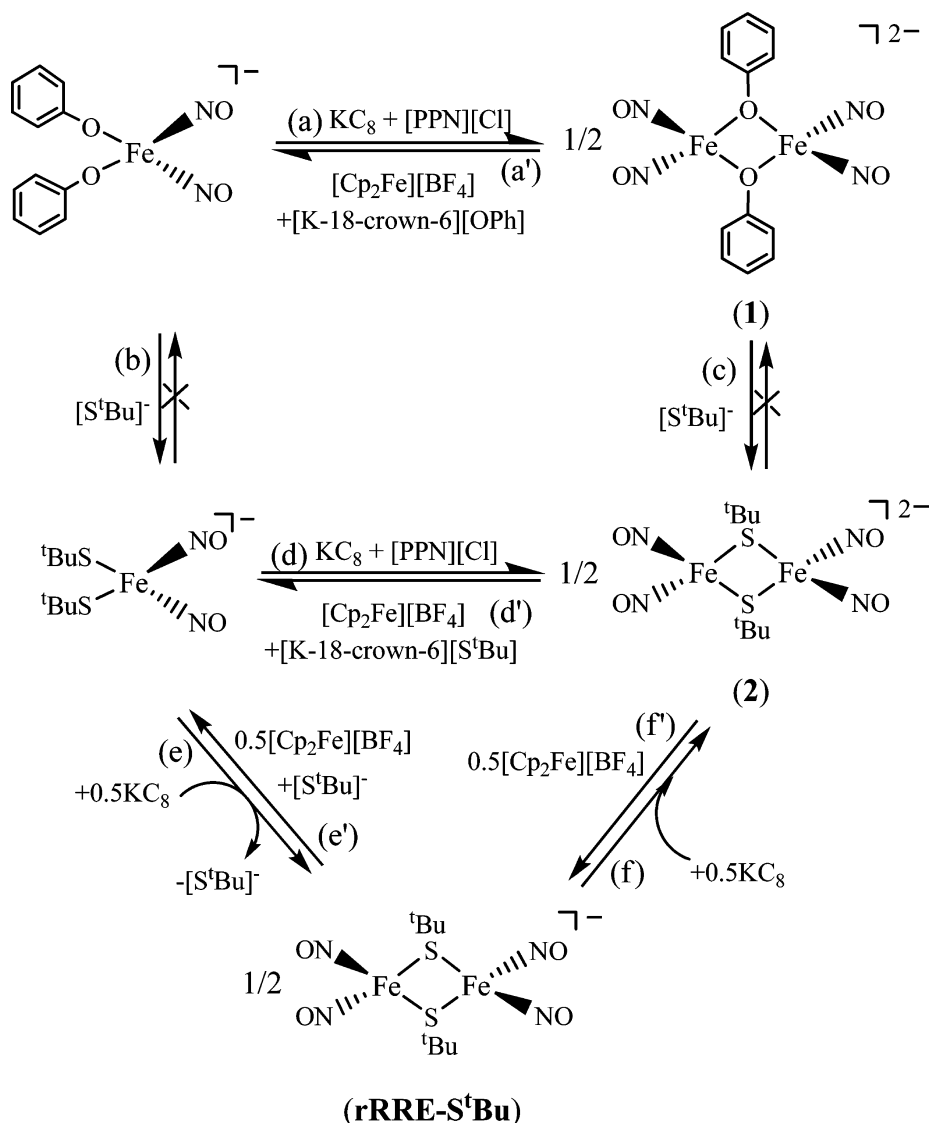
Dinitrosyliron complexes (DNICs) can act as the intrinsic NO-derived species that appear in various NO-producing tissues.¹ DNICs and S-nitrosothiols (RSNO) are known to be two possible forms for storage and delivery of NO in biological systems.² The interaction of NO with $[\text{Fe-S}]$ cluster-containing proteins in mitochondria, leading to the disassembly of the iron-sulfur core and the formation of DNICs as well as Roussin's red ester (RRE), has been well studied.^{1c,d} Also, nitrosylation of chelatable iron pool producing paramagnetic protein-bound DNICs has been observed.^{1e,f} DNICs displaying a distinctive electron paramagnetic resonance (EPR) signal at $g_{\text{av}} = 2.03$ have been adopted to characterize the formation of DNICs,^{2a,3} in addition to probing the formation of the $\{\text{Fe}(\text{NO})_2\}^9$ DNICs by the characteristic Fe K-edge preedge absorption energy (ranging from 7113.4 to 7113.8 eV) and nuclear resonance vibrational spectroscopy developed recently.^{3e,f} Although cysteine and glutathione have been proposed to be the major thiol components of cellular DNICs,^{1f,4} four

different kinds of potential coordinated ligands (cysteinate, histidine, deprotonated histidine, and tyrosinate) in protein-bound DNICs were proposed in enzymology.^{1d,3c,d} To our knowledge, the crystallographically characterized protein-bound DNIC containing mixed glutathione and tyrosinate ligands was demonstrated by the addition of a dinitrosyldiglutathionyliron complex into human glutathione S-transferase (GST) P1-1.⁵ The formation of protein-bound RREs accompanied by protein-bound DNICs (4:1 molar ratio) was observed through EPR and UV-vis spectra upon nitrosylation of the $[\text{4Fe-4S}]^{2+}$ clusters of FNR, a *hmp* gene transcription factor.⁶ RREs, the dimeric form of DNICs considered to perform a role similar to that of DNICs, are diamagnetic and EPR-silent because of the antiferromagnetic coupling between two Fe centers.⁷ We noticed that inactivation of mitochondrial aconitase by nitrosylation led to the formation of DNICs displaying the

Received: October 29, 2011

Published: March 9, 2012

Scheme 1



rhombic EPR spectrum with $g = 2.037, 2.031$, and 2.012 and an axial EPR spectrum with $g = 2.006$ and 1.97 assigned as a d^9 DNIC upon subsequent reduction by excess sodium dithionite.^{6b} In particular, reduction of the HiPIP-containing protein-bound DNIC and the protein-bound DNIC obtained from nitrosylation of $[2\text{Fe}-2\text{S}]^+$ in the SoxR revealed the same EPR spectrum as that proposed for d^9 DNIC.^{1c,6c}

In chemistry, mononuclear DNICs present various oxidation levels, including the EPR-active, anionic/neutral/cationic $\{\text{Fe}(\text{NO})_2\}^9$ DNICs $[(\text{NO})_2\text{FeL}_2]^{1-/0/+}$ ($\text{L} = \text{S/O/N/P}$ -containing ligands) as well as the EPR-silent, neutral $\{\text{Fe}(\text{NO})_2\}^{10}$ DNICs coordinated by CO, PPh_3 , and N-containing ligands.^{8–11} Here, the electronic state of the $\{\text{Fe}(\text{NO})_2\}^n$ core of DNICs is generally designated by Enemark–Feltham notation.¹² Because the small energy difference between transition-metal d and $\text{NO } \pi^*$ orbitals makes it complicated to define the “noninnocent” character of NO acting as NO^+ , NO , or NO^- .¹³ It is noticed that the dianionic $\{\text{Fe}(\text{NO})_2\}^{10}$ DNICs $[(\text{NO})_2\text{Fe}(\text{SC}_7\text{H}_4\text{SN})_2]^{2-}$ and $[(\text{NO})_2\text{Fe}(\text{OC}_7\text{H}_4\text{SN})_2]^{2-}$ coordinated by the weak σ -donor and π -acceptor ligands $[\text{SC}_7\text{H}_4\text{SN}]^-/[\text{OC}_7\text{H}_4\text{SN}]^-$ were reported recently.¹⁴ It implies that DNICs containing the $\{\text{Fe}(\text{NO})_2\}^9$

core, in certain cases, may exhibit a reversible one-electron reduction to produce the $\{\text{Fe}(\text{NO})_2\}^{10}$ state. On the basis of the oxidation levels of the $[\{\text{Fe}(\text{NO})_2\}\{\text{Fe}(\text{NO})_2\}]$ core of dinuclear DNICs, the dimeric DNICs can be classified into two different types: (i) the EPR-silent RRE with two $\{\text{Fe}(\text{NO})_2\}^9$ motifs stabilized by $\{\text{Fe}(\text{NO})_2\}^9-\{\text{Fe}(\text{NO})_2\}^9$ coupling^{7,15} and (ii) the EPR-active dinuclear DNICs with two $\{\text{Fe}(\text{NO})_2\}^9$ motifs stabilized by the delocalized mixed-valence $\{\text{Fe}(\text{NO})_2\}^{10}\{\text{Fe}(\text{NO})_2\}^9$ core.¹⁶ We also noticed that reduction of RREs yielding the proposed $[\text{Fe}(\mu\text{-SR})(\text{NO})_2]_2^-$ ($\text{R} = \text{Me, Et}$) with EPR $g = 1.995$ at 250 K and $[\text{Fe}(\mu\text{-SR})(\text{NO})_2]_2^{2-}$ characterized by IR and ^1H NMR were reported.¹⁷

In the previous report, we have established that the IR ν_{NO} in combination with EPR spectra may be employed to discriminate the $\{\text{Fe}(\text{NO})_2\}^9$ DNIC with a variety of coordinated ligands (S/N/O).^{7,8} The facile transformations and relative binding affinity of thiolate, imidazolate, phenolate, and nitrite toward the $\{\text{Fe}(\text{NO})_2\}^9$ motif were also investigated.^{3e} Conversion of $[(\text{NO})_2\text{Fe}(\mu\text{-SC}_6\text{H}_4\text{-}o\text{-NHCOPh})_2]$ into the neutral $\{\text{Fe}(\text{NO})_2\}^{10}$ DNIC $[(\text{NO})_2\text{Fe}(\text{PPh}_3)_2]$ via reductive elimination of the bridging thiolates was elucidated to be accessed by the π -acidic ligand, PPh_3 .^{7a} DNIC

$[(\text{RS})_2\text{Fe}(\text{NO})_2]^-$ and RRE $[\text{Fe}(\mu\text{-SR})(\text{NO})_2]_2$ ($\text{R} = \text{alkyl}$) are in dynamic equilibrium in protic solvent MeOH; subsequent chemical reduction of the DNIC and RRE mixture solution led to the formation of the reduced-form fully delocalized RRE $[\text{Fe}(\mu\text{-SR})(\text{NO})_2]_2^{2-}$ characterized by IR, UV-vis, EPR, SQUID, and single-crystal X-ray diffraction.¹⁶ Furthermore, the steric effect of thiolate ligands on interconversion among DNICs, RREs, and reduced-form RREs was also unraveled.^{16b} The addition of $\text{H}^+/\text{[SR]}^-$ to DNICs and RREs respectively triggered the interconversion of DNICs and RREs. In the present work, one-electron reduction of the anionic $\{\text{Fe}(\text{NO})_2\}^9$ DNIC $[(\text{NO})_2\text{Fe}(\text{OPh})_2]^-$ affording the $\{\text{Fe}(\text{NO})_2\}^{10}\{\text{Fe}(\text{NO})_2\}^{10}$ dianionic reduced RRE $[\text{Fe}(\mu\text{-OPh})(\text{NO})_2]_2^{2-}$ (**1**) and the transformation of the dianionic reduced RRE **1** into dianionic reduced RRE $[\text{Fe}(\mu\text{-S}^t\text{Bu})(\text{NO})_2]_2^{2-}$ (**2**) containing bridging thiolates were demonstrated. The reversible redox transformations $[(\text{NO})_2\text{Fe}(\text{S}^t\text{Bu})_2]^- \rightleftharpoons [\text{Fe}(\mu\text{-S}^t\text{Bu})(\text{NO})_2]_2^{2-} \rightleftharpoons [\text{Fe}(\mu\text{-S}^t\text{Bu})(\text{NO})_2]_2^- \rightleftharpoons [\text{Fe}(\mu\text{-S}^t\text{Bu})(\text{NO})_2]_2$ are elucidated. Of importance, the synthetic route to the $\{\text{Fe}(\text{NO})_2\}^{10}$ dianionic reduced monomeric DNIC $[\text{K}^+\text{-18-crown-6 ether}]_2[(\text{NO})_2\text{Fe}(\text{SEt})_2]$ (**3**) containing alkylthiolate-coordinated ligands was uncovered. The electronic features of $\{\text{Fe}(\text{NO})_2\}$ cores of complexes **1–3** were also discussed, on the basis of single-crystal X-ray structural data, EPR, density functional theory (DFT) computation, and X-ray absorption spectroscopy (XAS).

RESULTS AND DISCUSSION

Synthesis of $[\text{PPN}]_2[\text{Fe}(\mu\text{-OPh})(\text{NO})_2]_2$ (1**).** As shown in Scheme 1a, the treatment of $\{\text{Fe}(\text{NO})_2\}^9$ $[\text{PPN}][(\text{NO})_2\text{Fe}(\text{OPh})_2]$ with KC_8 and $[\text{PPN}][\text{Cl}]$ (1:1:1 molar ratio) in tetrahydrofuran (THF) at 0 °C led to the formation of the dianionic reduced RRE **1** bearing bridged phenoxides, characterized by IR, UV-vis spectroscopy, and single-crystal X-ray diffraction. Complex **1** exhibits diagnostic IR ν_{NO} stretching frequencies at 1651 s and 1602 s cm^{-1} (CH_3CN) with $Q_{\text{NO}} = 49 \text{ cm}^{-1}$ (Q_{NO} is the separation of NO stretching frequencies 1651 and 1602 cm^{-1}). The electronic absorption spectrum of complex **1** in CH_3CN displays absorptions at 272, 310, 381, and 854 nm at 300 K. Compared to the RREs with a $\{\text{Fe}(\text{NO})_2\}^9\text{--}\{\text{Fe}(\text{NO})_2\}^9$ coupling,¹⁶ the dianionic reduced RRE **1** is best described as a $\{\text{Fe}(\text{NO})_2\}^{10}\{\text{Fe}(\text{NO})_2\}^{10}$ core, which is responsible for the absence of paramagnetism and the EPR signal. It is presumed that one-electron reduction of $[(\text{NO})_2\text{Fe}(\text{OPh})_2]^-$ results in the buildup of the thermally unstable $\{\text{Fe}(\text{NO})_2\}^{10}$ $[(\text{NO})_2\text{Fe}(\text{OPh})_2]^{2-}$, which subsequently dimerizes to yield complex **1** via elimination of $[\text{OPh}]^-$. The failure to isolate the $\{\text{Fe}(\text{NO})_2\}^{10}$ dianionic reduced monomeric DNIC $[(\text{NO})_2\text{Fe}(\text{OPh})_2]^{2-}$ implies that the σ -donor ability of phenoxide stabilizes the $\{\text{Fe}(\text{NO})_2\}^9$ form,^{3e} while the known strong σ -donor and π -acceptor PPh_3 stabilizes the $\{\text{Fe}(\text{NO})_2\}^{10}$ form.^{7a,8d} No detectable quantities of the reduced form $[(\text{NO})_2\text{Fe}(\mu\text{-OPh})_2]^-$ were observed spectrally when $[(\text{NO})_2\text{Fe}(\text{OPh})_2]^-$ was dissolved in MeOH at ambient temperature, in contrast to dissolution of $[(\text{NO})_2\text{Fe}(\text{SEt})_2]^-$ in MeOH, finally leading to the formation of a mixture of the reduced form RRE $[(\text{NO})_2\text{Fe}(\mu\text{-SEt})_2]^-$ and $[(\text{NO})_2\text{Fe}(\text{SEt})_2]^-$ observed in the previous study.¹⁶

Reversibly, conversion of complex **1** into $[(\text{NO})_2\text{Fe}(\text{OPh})_2]^-$ under the presence of $[\text{Cp}_2\text{Fe}][\text{BF}_4]$ and $[\text{K-18-crown-6 ether}][\text{OPh}]$ was displayed and monitored by IR ν_{NO} spectra (Scheme 1a'). The shift of NO stretching frequencies

from (1651 s, 1602 s cm^{-1}) to (1747 m, 1681 s cm^{-1}) was consistent with the formation of the $\{\text{Fe}(\text{NO})_2\}^9$ DNIC $[(\text{NO})_2\text{Fe}(\text{OPh})_2]^-$ when the CH_3CN solution of complex **1** was reacted with $[\text{Cp}_2\text{Fe}][\text{BF}_4]$ and $[\text{K-18-crown-6 ether}][\text{OPh}]$ in a 1:2:2 molar ratio (Scheme 1a'). The absence of the formation of the $\{\text{Fe}(\text{NO})_2\}^{10}\{\text{Fe}(\text{NO})_2\}^9$ reduced form RRE $[(\text{NO})_2\text{Fe}(\mu\text{-OPh})_2]^-$ suggests that a concerted two-electron oxidation along with the nucleophilic attack of $[\text{OPh}]^-$ on two Fe centers occurs upon the transformation of complex **1** into $[(\text{NO})_2\text{Fe}(\text{OPh})_2]^-$ triggered by $[\text{Cp}_2\text{Fe}][\text{BF}_4]$ and $[\text{OPh}]^-$. That is, oxidation of complex **1** is presumed to occur only at the more accessible, electron-rich Fe sites. Obviously, complexes $[(\text{NO})_2\text{Fe}(\text{OPh})_2]^-$ and **1** are chemically interconvertible.

Synthesis of $[\text{PPN}]_2[\text{Fe}(\mu\text{-S}^t\text{Bu})(\text{NO})_2]_2$ (2**).** Compared to the stronger electron-donating thiolate $[\text{S}^t\text{Bu}]^-$ triggering ligand exchange of $\{\text{Fe}(\text{NO})_2\}^9$ $[(\text{NO})_2\text{Fe}(\text{OPh})_2]^-$ to produce the thermally stable $\{\text{Fe}(\text{NO})_2\}^9$ $[(\text{NO})_2\text{Fe}(\text{S}^t\text{Bu})_2]^-$ (Scheme 1b),^{3e} quantitative transformation of complex **1** to the $\{\text{Fe}(\text{NO})_2\}^{10}\{\text{Fe}(\text{NO})_2\}^{10}$ **2** was demonstrated upon the addition of 2 equiv of $[\text{S}^t\text{Bu}]^-$ to a CH_3CN solution of complex **1** (Scheme 1c). The surprisingly stable complex **2** is the first example of the dianionic reduced RREs containing the bridging thiolates coordinated to the $\{\text{Fe}(\text{NO})_2\}^{10}\{\text{Fe}(\text{NO})_2\}^{10}$ motif isolated and characterized by IR, UV-vis, XAS, and single-crystal X-ray diffraction. The lower-energy ν_{NO} bands of complex **2** [1637 m, 1613 s, 1578 s, 1567 s cm^{-1} (KBr)] shifted by $\sim 30 \text{ cm}^{-1}$ from those of complex **1** demonstrated the conversion of complex **1** into complex **2**.¹⁸ In contrast to the reduced RRE $[(\text{NO})_2\text{Fe}(\mu\text{-S}^t\text{Bu})_2]^-$ (**rRRE-S}^t\text{Bu}**) displaying an intense intervalence transition absorption around 982 nm, the UV-vis spectrum of complex **2** displays absorptions 270 and 396 nm (CH_3CN).¹⁶ Presumably, the conversion of complex **1** into complex **2** is ascribed to the capability of thiolate to bridge two $\{\text{Fe}(\text{NO})_2\}^{10}$ fragments and the preference of $\{\text{Fe}(\text{NO})_2\}^{10}$ motifs to be connected by the electron-donating (soft) thiolate. Obviously, $[\text{OPh}]^-$ and $[\text{S}^t\text{Bu}]^-$ rendering the $\{\text{Fe}(\text{NO})_2\}^{10}$ unit in different electronic environments induce different stabilities to the $\{\text{Fe}(\text{NO})_2\}^{10}\{\text{Fe}(\text{NO})_2\}^{10}$ motif. This result concludes that the binding preference for a given ligand ($[\text{OPh}]^-$ and $[\text{SR}]^-$) of the $\{\text{Fe}(\text{NO})_2\}^{10}\{\text{Fe}(\text{NO})_2\}^{10}$ motif of dianionic reduced RREs follows the ligand-displacement series $[\text{SR}]^- > [\text{OPh}]^-$, consistent with the binding preference for the ligand of the $\{\text{Fe}(\text{NO})_2\}^9$ motif of DNICs.^{3e}

As presented in Scheme 1d,d', when $\text{KC}_8 + [\text{PPN}][\text{Cl}]$ was added to the THF solution of complex $[\text{PPN}][(\text{NO})_2\text{Fe}(\text{S}^t\text{Bu})_2]$ with a 1:1:1 stoichiometry at 0 °C, transformation of the DNIC $[\text{PPN}][(\text{NO})_2\text{Fe}(\text{S}^t\text{Bu})_2]$ into complex **2** was observed and monitored by IR ν_{NO} spectroscopy; the shift in the ν_{NO} stretching frequencies from 1721 m and 1676 s cm^{-1} (KBr) to 1637 m, 1613 s, 1578 s, and 1567 s cm^{-1} (KBr) confirmed the formation of complex **2**.¹⁸ As proposed in the transformation of $[(\text{NO})_2\text{Fe}(\text{OPh})_2]^-$ into complex **1**, the reasonable assumption that the $\{\text{Fe}(\text{NO})_2\}^{10}$ dianionic reduced monomeric DNIC $[\text{PPN}]_2[(\text{NO})_2\text{Fe}(\text{S}^t\text{Bu})_2]$ is the kinetic product that isomerizes into the more stable dianionic reduced RRE $\{\text{Fe}(\text{NO})_2\}^{10}\{\text{Fe}(\text{NO})_2\}^{10}$ complex **2** via elimination of $[\text{S}^t\text{Bu}]^-$. Reversibly, the formation of the DNIC $[\text{PPN}][(\text{NO})_2\text{Fe}(\text{S}^t\text{Bu})_2]$ was observed upon the addition of 2 equiv of $[\text{Cp}_2\text{Fe}][\text{BF}_4] + [\text{K-18-crown-6 ether}][\text{S}^t\text{Bu}]$ to the CH_3CN solution of complex **2** at ambient temperature. The electrochemistry of complex **2**, measured in CH_3CN with 0.1 M $[\text{nBu}_4\text{N}][\text{PF}_6]$ as supporting electrolyte at room temperature

(scan rate 500 mV/s), reveals two reversible oxidation–reduction processes at -0.99 and -1.61 V ($E_{1/2}$; vs $\text{Cp}_2\text{Fe}/\text{Cp}_2\text{Fe}^+$), respectively (Figure 1). For $E_{1/2} = -1.61$ V, complex

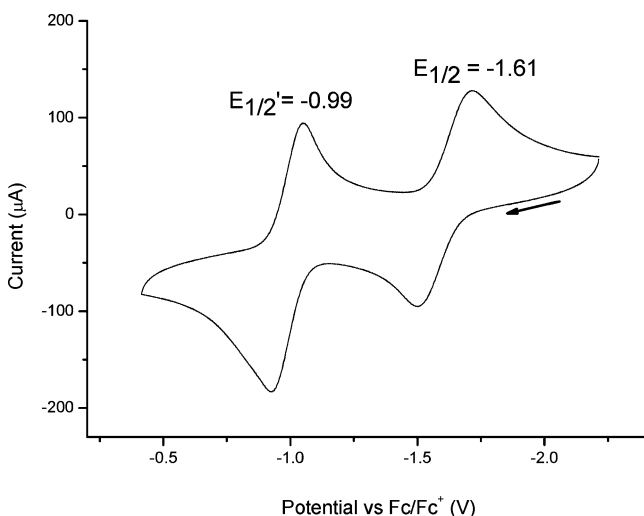


Figure 1. Cyclic voltammogram of complex **2** in a 2.5 mM CH_3CN solution with 0.1 M $[\text{nBu}_4\text{N}][\text{PF}_6]$ as the supporting electrolyte at room temperature (scan rate 0.5 V/s). The arrow indicates the direction of the scan.

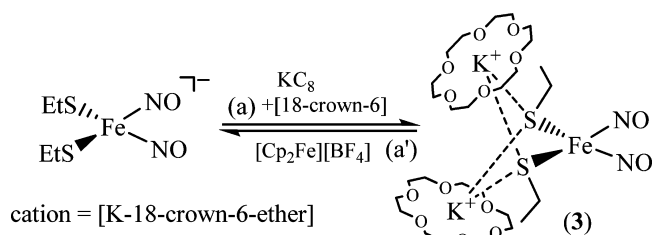
2 undergoes one-electron oxidation ($\Delta E_p = 213$ mV; $i_{pa}/i_{pc} = 0.82$) to a mixed-valence $\{\text{Fe}(\text{NO})_2\}^{\text{I}}\{\text{Fe}(\text{NO})_2\}^{\text{II}}$ species, which can be further oxidized to a $\{\text{Fe}(\text{NO})_2\}^{\text{II}}\{\text{Fe}(\text{NO})_2\}^{\text{III}}$ species at $E_{1/2} = -0.99$ V ($\Delta E_p = 122$ mV; $i_{pa}/i_{pc} = 1.08$). In contrast, the cyclic voltammogram of complex **1** with bridging phenoxides displays an irreversible oxidation at -0.44 and -1.04 V (vs $\text{Cp}_2\text{Fe}/\text{Cp}_2\text{Fe}^+$) at 298 K [scan rate 1 V/s; Figure S1 in the Supporting Information (SI)].

In a similar fashion, upon the addition of KC_8 and $[\text{PPN}][\text{Cl}]$ to the THF solution of the DNIC $[\text{PPN}][(\text{NO})_2\text{Fe}(\text{S}^t\text{Bu})_2]$ in a 1:1:2 molar ratio, a pronounced color change from red-brown to dark-green occurred at ambient temperature. IR, UV–vis, and EPR confirmed the formation of the known $[\text{Fe}(\mu\text{-S}^t\text{Bu})(\text{NO})_2]_2^-$ (**rRRE-S^tBu**; Scheme 1e).¹⁶ This result implies that the presumed thermally unstable $\{\text{Fe}(\text{NO})_2\}^{\text{I}}\text{DNIC}$ $[\text{PPN}]_2[(\text{NO})_2\text{Fe}(\text{S}^t\text{Bu})_2]$ derived from the reduction of $[(\text{NO})_2\text{Fe}(\text{S}^t\text{Bu})_2]^-$ may lead to the buildup of the coordination-unsaturated $\{\text{Fe}(\text{NO})_2\}^{\text{I}}[(\text{NO})_2\text{Fe}(\text{S}^t\text{Bu})_2]^-$ intermediate via elimination of $[\text{S}^t\text{Bu}]^-$. The subsequent coordinative association of $\{\text{Fe}(\text{NO})_2\}^{\text{I}}[(\text{NO})_2\text{Fe}(\text{S}^t\text{Bu})_2]^-$ and $\{\text{Fe}(\text{NO})_2\}^{\text{I}}[(\text{NO})_2\text{Fe}(\text{S}^t\text{Bu})_2]^-$ accompanied by the concurrent elimination of $[\text{S}^t\text{Bu}]^-$ affords **rRRE-S^tBu**. The reaction sequences accounting for the transformation of $[(\text{NO})_2\text{Fe}(\text{S}^t\text{Bu})_2]^-$ into **rRRE-S^tBu** described above suggest that the metastable $\{\text{Fe}(\text{NO})_2\}^{\text{I}}[(\text{NO})_2\text{Fe}(\text{S}^t\text{Bu})_2]^{2-}$ intermediate may be isolated, in contrast to the reduction of $[(\text{NO})_2\text{Fe}(\text{O}^i\text{Pr})_2]^-$. That is, the $[\text{S}^t\text{Bu}]^-$ -coordinated ligand may function to stabilize the $\{\text{Fe}(\text{NO})_2\}^{\text{I}}$ DNICs, compared to $[\text{O}^i\text{Pr}]^-$ -coordinated ligand.^{7a,8d} The complete conversion of complex **rRRE-S^tBu** to complex **2** was observed when complex **rRRE-S^tBu**, KC_8 , and 18-crown-6 ether were dissolved in THF and stirred at 0 °C for 10 min (Scheme 1f). Here, the reduction of complex **rRRE-S^tBu** is presumed to mainly occur at the redox-active Fe sites to afford complex **2**. Obviously, $[\text{Fe}(\mu\text{-S}^t\text{Bu})(\text{NO})_2]_2$, **rRRE-S^tBu**, and complex **2** are chemically

reversible via redox processes (d–d', e–e', and f–f' of Scheme 1).

Synthesis of $[\text{K-18-crown-6 ether}]_2[(\text{NO})_2\text{Fe}(\text{SEt})_2]$ (3**).** In contrast to reduction of the $\{\text{Fe}(\text{NO})_2\}^{\text{I}}$ DNIC $[\text{PPN}][(\text{NO})_2\text{Fe}(\text{S}^t\text{Bu})_2]$ yielding the $\{\text{Fe}(\text{NO})_2\}^{\text{I}}\{\text{Fe}(\text{NO})_2\}^{\text{I}}$ complex **2**, the $\{\text{Fe}(\text{NO})_2\}^{\text{I}}$ DNIC $[\text{K-18-crown-6 ether}][(\text{NO})_2\text{Fe}(\text{SEt})_2]$ reacted upon time of mixing with 1 equiv of $[\text{KC}_8] + [\text{18-crown-6 ether}]$ to yield cleanly the $\{\text{Fe}(\text{NO})_2\}^{\text{II}}$ dianionic reduced monomeric DNIC **3** in THF at 0 °C, where preservation of the mononuclear $\{\text{Fe}(\text{NO})_2\}^{\text{II}}$ DNIC (vs dimerization, yielding the dinuclear **2**) depends on the choice of the cation (Scheme 2a). Complex **3**, characterized by IR,

Scheme 2



UV–vis, and single-crystal X-ray diffraction, is extremely air-sensitive in solid state and THF solutions. Reduction of $\{\text{Fe}(\text{NO})_2\}^{\text{I}}$ $[\text{K-18-crown-6 ether}][(\text{NO})_2\text{Fe}(\text{SEt})_2]$ at 0 °C, yielding the $\{\text{Fe}(\text{NO})_2\}^{\text{II}}$ DNIC **3**, is also characterized by significant decreases in the ν_{NO} value ($\Delta\nu_{\text{NO}} \sim 100$ cm^{-1}) and shifts of the IR ν_{NO} stretching frequencies from (1715 m, 1673 s cm^{-1}) to (1614 m, 1571 s cm^{-1}) (THF). The lower-energy NO bands of complex **3** are shifted by ~ 100 cm^{-1} from those of the $\{\text{Fe}(\text{NO})_2\}^{\text{I}}$ DNIC $[\text{K-18-crown-6 ether}][(\text{NO})_2\text{Fe}(\text{SEt})_2]$. Known to serve as a reporter of the electron density at Fe similarly to CO,¹⁹ the shift in the NO frequencies reflects a variation in the electronic structure of $\{\text{Fe}(\text{NO})_2\}$ motif, that is, $\{\text{Fe}(\text{NO})_2\}^{\text{I}} \rightarrow \{\text{Fe}(\text{NO})_2\}^{\text{II}}$. Here, reduction of the DNIC $[(\text{NO})_2\text{Fe}(\text{SEt})_2]^-$ yielding complex **3** is presumed to occur mainly at the Fe site. The $\{\text{Fe}(\text{NO})_2\}^{\text{II}}$ DNIC **3** containing intermolecular $\text{Fe}(\text{SR})_2 \cdots (\text{K}^+)_2$ interactions was verified by single-crystal X-ray diffraction in the solid state. Presumably, the electronic perturbation caused by reduction of the $\{\text{Fe}(\text{NO})_2\}^{\text{I}}$ DNIC $[\text{K-18-crown-6 ether}][(\text{NO})_2\text{Fe}(\text{SEt})_2]$ triggers the intermolecular $[\text{Fe}(\text{SR})_2 \cdots (\text{K}^+)_2]$ interactions to diminish the electronic donation from $[\text{SEt}]^-$ to the Fe center to stabilize the $\{\text{Fe}(\text{NO})_2\}^{\text{II}}$ DNIC **3**. Obviously, the formation of alkylthiolate-containing $\{\text{Fe}(\text{NO})_2\}^{\text{II}}$ DNICs $[(\text{NO})_2\text{Fe}(\text{SEt})_2]^{2-}$ can be obtained by modulating the thiolate electron-donation strength through $[(\text{SR})^- \cdots \text{cation}]$ interactions. The UV–vis spectrum of the DNIC **3** exhibits intense absorption bands at 370 and 423 nm (THF). Because of the absence of the EPR signal, the DNIC **3** was characterized as a diamagnetic species. Reversibly, the reaction of the oxidant $[\text{Cp}_2\text{Fe}][\text{BF}_4]$ with the DNIC **3** in CH_3CN at 0 °C yielded the dark-brown solution whose IR ν_{NO} suggested formulation as the known $[\text{K-18-crown-6 ether}][(\text{NO})_2\text{Fe}(\text{SEt})_2]$, as shown in Scheme 2a.¹⁶ These results illustrate one aspect of how the countercation of the anionic $\{\text{Fe}(\text{NO})_2\}^{\text{I}}$ DNICs functions to control the formation of the $\{\text{Fe}(\text{NO})_2\}^{\text{II}}$ dianionic reduced monomeric DNICs or the $\{\text{Fe}(\text{NO})_2\}^{\text{I}}\{\text{Fe}(\text{NO})_2\}^{\text{I}}$ dianionic reduced RREs upon reduction of the $\{\text{Fe}(\text{NO})_2\}^{\text{I}}$ DNICs $[\text{cation}][(\text{NO})_2\text{Fe}(\text{SR})_2]$ (cation = K^+ -18-crown-6 ether, PPN^+).

Structure. Figure 2 shows the thermal ellipsoid plot of complex **1**, and selected bond dimensions are presented in the

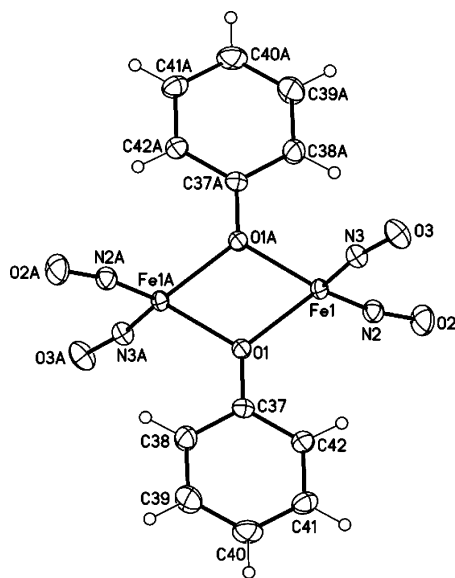


Figure 2. ORTEP drawing and labeling scheme of complex **1** with thermal ellipsoids drawn at 50% probability. Selected bond distances (Å) and angles (deg): Fe1...Fe1A 3.261(1), Fe1–N2 1.654(1), Fe1–N3 1.654(1), Fe1–O1 2.027(1), Fe1–O1A 2.031(1), N2–O2 1.209(2), N3–O3 1.211(2); N2–Fe1–N3 111.4(1), N2–Fe1–O1 118.3(1), N3–Fe1–O1 117.3(1), N2–Fe1–O1A 116.1(1), N3–Fe1–O1A 115.9(1), O1–Fe1–O1A 73.1(1), O2–N2–Fe1 165.2(1), O3–N3–Fe1 163.8(1), Fe1–O1–Fe1A 106.9(1).

figure caption. The symmetrical structure of complex **1** possesses D_{2h} symmetry, and the local environment of the Fe center exhibits a distorted tetrahedral geometry. The $[\text{Fe}(\mu\text{-O})_2\text{Fe}]$ core geometry of complex **1** is best described as a planar rhombus, with two phenyl groups adopting a coplanar configuration in the solid state. The apparently longer Fe(1)···Fe(1A) distance [3.261(1) Å], presumably, attenuates the Fe···Fe interaction to relieve the richness of the electron density surrounding the $\{\text{Fe}(\text{NO})_2\}^{10}\{\text{Fe}(\text{NO})_2\}^{10}$ $[\text{Fe}(\mu\text{-O})_2\text{Fe}]$ core (Table 1).¹⁶ The mean Fe–N [1.654(1) Å] and N–O [1.210(2) Å] bond distances nearly fall within the range

of $\{\text{Fe}(\text{NO})_2\}^{10}$ DNICs [1.650(7)–1.638(3) Å for Fe–N and 1.214(6)–1.189(4) Å for N–O].^{8d}

The molecular structure of complex **2** in $[\text{PPN}]^+$ salt is depicted in Figure 3, and the selected bond distances and

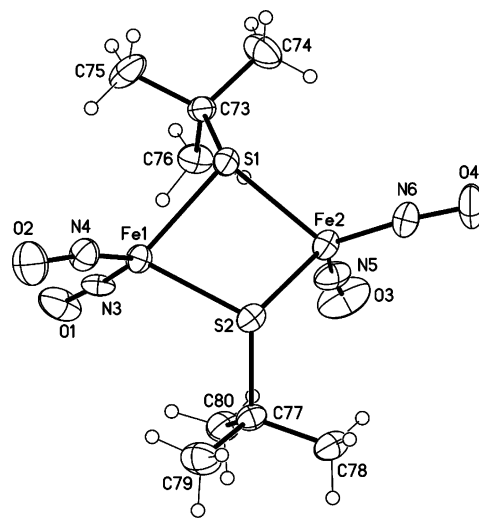


Figure 3. ORTEP drawing and labeling scheme of complex **2** with thermal ellipsoids drawn at 50% probability. Selected bond distances (Å) and angles (deg): Fe1...Fe2 3.437(1), Fe1–N3 1.610(3), Fe1–N4 1.660(3), Fe1–S1 2.363(1), Fe1–S2 2.348(1), N3–O1 1.245(3), N4–O2 1.216(3); N3–Fe1–N4 115.2(1), N3–Fe1–S1 112.2(1), N3–Fe1–S2 118.3(1), N4–Fe1–S2 108.2(1), N4–Fe1–S1 119.1(1), S2–Fe1–S1 79.05(3), O1–N3–Fe1 173.3(3), O2–N4–Fe1 160.6(3), Fe2–S1–Fe1 93.60(3).

angles are presented in the figure caption. The geometry of the $[\text{Fe}(\mu\text{-S})_2\text{Fe}]$ core in complex **2** is best portrayed as a butterfly-like structure with two *tert*-butyl groups adopting a syn configuration and a dihedral angle of 139° (the intersection of two $[\text{Fe}_2\text{S}]$ planes) in the solid state. The geometrical change of the $[\text{Fe}(\mu\text{-S})_2\text{Fe}]$ core from a planar rhombus to a butterfly-like structure occurs upon going from a $\{\text{Fe}(\text{NO})_2\}^{10}\{\text{Fe}(\text{NO})_2\}^{10}$ electronic structure of complex $[(\text{NO})_2\text{Fe}(\mu\text{-S}^t\text{Bu})_2]_2$ and a $\{\text{Fe}(\text{NO})_2\}^{10}\{\text{Fe}(\text{NO})_2\}^{10}$ electronic structure of complex **rRRE-S^tBu** to a $\{\text{Fe}(\text{NO})_2\}^{10}\{\text{Fe}(\text{NO})_2\}^{10}$ electronic structure of complex **2**. As shown in Table 1, the different oxidation

Table 1. Selected Metric Data for $[\text{Fe}(\mu\text{-S}^t\text{Bu})(\text{NO})_2]_2$,^{15b} **rRRE-S^tBu**,¹⁶ **1**, and **2**

	$[\text{Fe}(\mu\text{-S}^t\text{Bu})(\text{NO})_2]_2$	rRRE-S^tBu	2	1
Fe···Fe (Å)	2.705(1)	2.958(1)	3.437(1)	3.261(1)
Fe–S (Å) ^a	2.253(1)	2.303(1)	2.348(1)	
Fe–O (Å) ^a				2.029(1)
Fe–N (Å) ^a	1.668(1)	1.662(2)	1.637(3)	1.654(1)
N–O (Å) ^a	1.169(2)	1.186(3)	1.223(3)	1.210(2)
S···S (Å)	3.604(1)	3.531(1)	2.998(1)	
O···O (Å)				2.416(1)
∠Fe–S–Fe (deg)	73.78(2)	79.89(3)	94.11(3) ^a	
∠Fe–O–Fe (deg)				106.92(5)
∠S–Fe–S (deg)	106.22(2)	100.11(3)	79.36(3) ^a	
∠O–Fe–O (deg)				73.08(5)
∠N–Fe–N (deg) ^a	116.58(10)	116.08(12)	115.32(14)	111.35(6)
∠Fe–N–O (deg) ^a	169.01(14)	169.5(2)	167.7(3)	164.49(11)
dihedral ∠ (deg) ^b	180	180	139	180

^aAverage bond distance and angle. ^bDefined by the intersection of two $[\text{Fe}_2\text{S}]$ or $[\text{Fe}_2\text{O}]$ planes.

levels of complexes $[(\text{NO})_2\text{Fe}(\mu\text{-S}^t\text{Bu})]_2$, **rRRE-S^tBu**, and **2** display the distinctly different Fe⋯Fe distances, 2.705(1) Å for $[(\text{NO})_2\text{Fe}(\mu\text{-S}^t\text{Bu})]_2$,^{15b} 2.958(1) Å for **rRRE-S^tBu**, and 3.437(1) Å for complex **2**.¹⁶ Specifically, the lengthening of the Fe⋯Fe distance of complex **2**, compared to those of the $\{\text{Fe}(\text{NO})_2\}_2^9\{\text{Fe}(\text{NO})_2\}_2^9[(\text{NO})_2\text{Fe}(\mu\text{-S}^t\text{Bu})]_2$ and the $\{\text{Fe}(\text{NO})_2\}_2^{10}\{\text{Fe}(\text{NO})_2\}_2^9$ **rRRE-S^tBu**, is employed to relieve the electronic richness induced by reduction of the $\{\text{Fe}(\text{NO})_2\}_2^{10}\{\text{Fe}(\text{NO})_2\}_2^9$ **rRRE-S^tBu** to stabilize complex **2**. Such geometrical differences [planar rhombus vs butterfly-like structure and Fe⋯Fe distance of 2.705(1) Å for $[(\text{NO})_2\text{Fe}(\mu\text{-S}^t\text{Bu})]_2$ vs 3.437(1) Å for complex **2**], as determined by the electronic structures of $[(\text{NO})_2\text{Fe}(\mu\text{-S}^t\text{Bu})]_2$, **rRRE-S^tBu**, and complex **2**, demand ligands capable of matching the geometrical requirement of the $[\text{Fe}(\mu\text{-S})_2\text{Fe}]$ core as well as maintaining an optimum electronic condition, cooperatively regulated by the noninnocent NO ligands, to stabilize the dinuclear DNICs. The lengthening of the average Fe–S bond lengths from 2.253(1) Å for $[(\text{NO})_2\text{Fe}(\mu\text{-S}^t\text{Bu})]_2$ and 2.303(1) Å for **rRRE-S^tBu** to 2.348(1) Å for complex **2** is presumably caused by an electronic perturbation from the $\{\text{Fe}(\text{NO})_2\}_2^9$ and $\{\text{Fe}(\text{NO})_2\}_2^{10}\{\text{Fe}(\text{NO})_2\}_2^9$ cores of complexes $[(\text{NO})_2\text{Fe}(\mu\text{-S}^t\text{Bu})]_2$ and **rRRE-S^tBu**, respectively, to the $\{\text{Fe}(\text{NO})_2\}_2^{10}\{\text{Fe}(\text{NO})_2\}_2^{10}$ core of complex **2** (Table 1). Because of the increase of electron back-donation from the $\{\text{Fe}(\text{NO})_2\}_2^{10}\{\text{Fe}(\text{NO})_2\}_2^{10}$ core to NO ligands, the reduction of **rRRE-S^tBu** yielding complex **2** is believed to cause the bending of the mean Fe–N–O bond angles [mean Fe–N–O bond angle: 169.5(2)° for **rRRE-S^tBu** and 167.7(3)° for complex **2**] (Table 1). Also, the average N–O bond length of 1.223(3) Å and the average Fe–N bond distance of 1.637(3) Å fall out of the published N–O and Fe–N bond lengths of $\{\text{Fe}(\text{NO})_2\}_2^{10}$ DNICs [1.214(6)–1.189(4) Å for N–O and 1.650(7)–1.638(3) Å for Fe–N].^{8d} That is, a dominant $\{\text{Fe}^{\text{II}}(\text{NO})_2\}_2^{10}\{\text{Fe}^{\text{II}}(\text{NO})_2\}_2^{10}$ electronic structure, modulated by the redox-active Fe centers and noninnocent NO ligands, is proposed for complexes **1** and **2**.^{3e,12b}

As shown in Figure 4, analysis of the bond angles [N1–Fe–N2 115.3(2)° and S1–Fe–S2 87.64(4)°] of complex **3** reveals that Fe is best described as existing in a distorted tetrahedral coordination environment because of the intermolecular $[\text{Fe}(\text{SR})_2\cdots(\text{K}^+)]_2$ interactions, with the average (RS)⋯K⁺ distance of 3.277(2) Å [S1⋯K1 3.265(2) Å and S2⋯K2 3.288(1) Å]. Also, each K⁺ is additionally coordinated to one 18-crown-6 ether. The mean N–O bond distance of 1.205(4) Å [1.203(4) and 1.206(3) Å] in complex **3** approaches the upper end of 1.189(4)–1.214(6) Å for the neutral $\{\text{Fe}(\text{NO})_2\}_2^{10}$ DNICs; meanwhile, the mean Fe–N(O) distance of 1.642(4) Å [1.638(4) and 1.646(4) Å] in complex **3** falls in the range reported for $\{\text{Fe}(\text{NO})_2\}_2^{10}$ DNICs.^{8d} Of importance, it is noticed that the Fe1–N1–O1 and Fe2–N2–O2 bond angles of 170.4(3)° and 165.1(3)°, respectively, in complex **3** are distinctive from the mean Fe–N–O bond angle of 172.1° in the $\{\text{Fe}(\text{NO})_2\}_2^9[(\text{NO})_2\text{Fe}(\text{SEt})_2]_2$.^{8e}

XAS. The Fe K-edge spectra of a series of monomeric $\{\text{Fe}(\text{NO})_2\}_2^{10}$ DNICs and dinuclear $\{\text{Fe}(\text{NO})_2\}_2^{10}\{\text{Fe}(\text{NO})_2\}_2^{10}$ DNICs are shown in Figures 5 and 6, Figures S2–S4 in the SI, and Table 2. The preedge transition is due to the d–p mixing of the distorted T_d local environment of the Fe center.^{8a} Compared to the tetrahedral $\{\text{Fe}(\text{NO})_2\}_2^9$ DNIC $[(\text{NO})_2\text{Fe}(\text{OPh})_2]^-$ (7113.7 eV),^{3c} complex **1** exhibiting a lower preedge energy at 7113.3 eV may suggest that the effective nuclear charge (Z_{eff}) of Fe in complex **1** is lower than that of

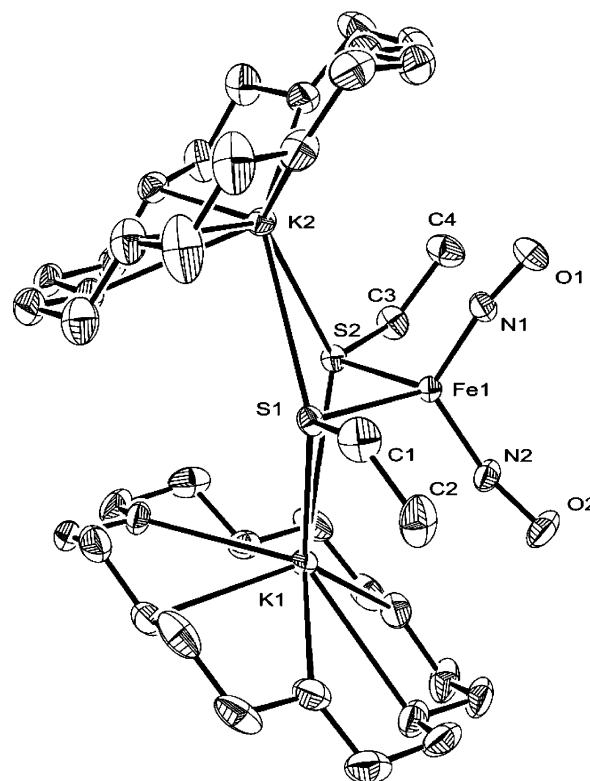


Figure 4. ORTEP drawing and labeling scheme of complex **3** with thermal ellipsoids drawn at 50% probability. Selected bond distances (Å) and angles (deg): Fe1–N1 1.638(4), Fe1–N2 1.646(4), Fe1–S1 2.315(1), Fe1–S2 2.332(1), N1–O1 1.203(4), N2–O2 1.206(3), S1⋯K1 3.265(2), S2⋯K2 3.288(1); N1–Fe1–N2 115.3(2), N1–Fe1–S1 108.1(1), N2–Fe1–S2 114.4(1), N1–Fe1–S2 116.9(1), N2–Fe1–S1 110.6(1), S1–Fe1–S2 87.64(4), O1–N1–Fe1 170.4(3), O2–N2–Fe1 165.1(3).

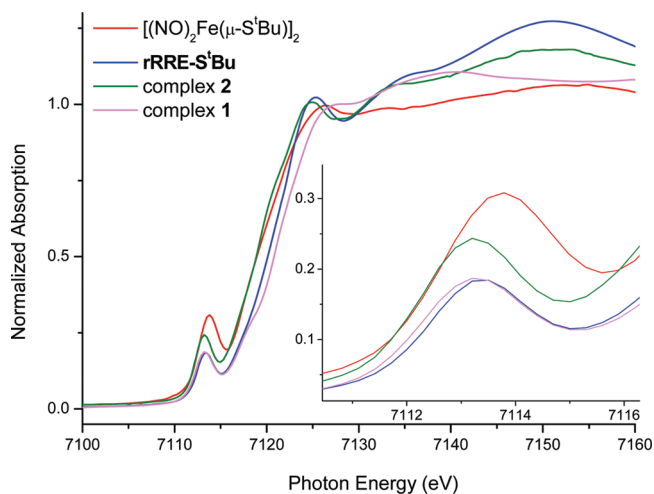


Figure 5. XAS Fe K-edge spectra of complexes **1**, **2**, **rRRE-S^tBu**, and $[(\text{NO})_2\text{Fe}(\mu\text{-S}^t\text{Bu})]_2$.

$[(\text{NO})_2\text{Fe}(\text{OPh})_2]^-$. The Fe K-edge preedge energies of the isolectic complexes $[(\text{NO})_2\text{Fe}(\text{OPh})_2]^-$ and **1** containing similar coordination geometries may be used as a marker of the oxidation state of the Fe center.²⁰ Because the theoretical computations as well as the Fe K-edge preedge energy define the electronic structure of the $\{\text{Fe}(\text{NO})_2\}_2^9$ core of the mononuclear DNIC $[(\text{NO})_2\text{Fe}(\text{OPh})_2]^-$ as

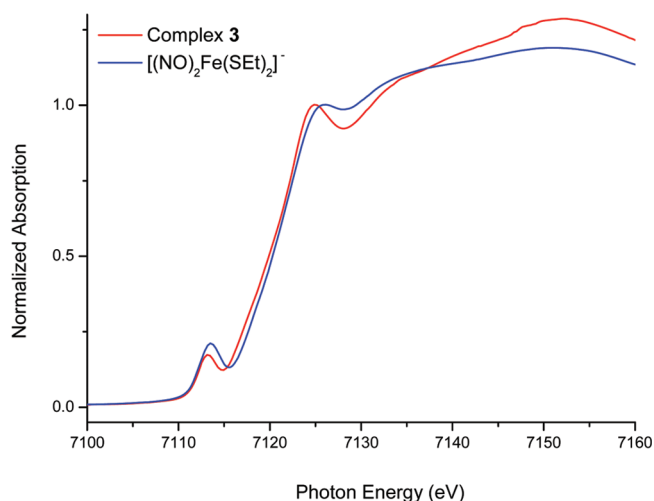


Figure 6. XAS Fe K-edge spectra of complexes 3 and $[(\text{NO})_2\text{Fe}(\text{SET})_2]^-$.

Table 2. XAS Preedge Energies for DNICs 1–3, $\text{rRRE-S}^t\text{Bu}$, $[(\text{NO})_2\text{Fe}(\mu\text{-S}^t\text{Bu})_2]$, $[(\text{NO})_2\text{Fe}(\text{SET})_2]^-$, $[(\text{NO})_2\text{Fe}(\text{OPh})_2]^-$, $[(\text{PPh}_3)_2\text{Fe}(\text{NO})_2]$, $[(\text{Sparteine})\text{Fe}(\text{NO})_2]$, $[(\text{TMEDA})\text{Fe}(\text{NO})_2]$, $[(-\text{SC}_7\text{H}_4\text{SN})_2\text{Fe}(\text{NO})_2]^{1-/2-}$, and $[(\text{OC}_7\text{H}_4\text{SN}-)_2\text{Fe}(\text{NO})_2]^{1-/2-}$

compound	first derivative ($d\mu/dE = 0$) preedge peak	reference
$\{\text{Fe}(\text{NO})_2\}_2^{10}\{\text{Fe}(\text{NO})_2\}_2^{10}$		
1	7113.3	this work
2	7113.2	this work
$\{\text{Fe}(\text{NO})_2\}_2^{10}\{\text{Fe}(\text{NO})_2\}_2^9$		
rRRE-S^tBu	7113.4	16
$\{\text{Fe}(\text{NO})_2\}_2^9\{\text{Fe}(\text{NO})_2\}_2^9$		
$[(\text{NO})_2\text{Fe}(\mu\text{-S}^t\text{Bu})_2]$	7113.8	15b
$\{\text{Fe}(\text{NO})_2\}_2^{10}$		
3	7113.2	this work
$[(\text{Sparteine})\text{Fe}(\text{NO})_2]$	7113.2	8d
$[(\text{TMEDA})\text{Fe}(\text{NO})_2]$	7113.1	8d
$[(-\text{SC}_7\text{H}_4\text{SN})_2\text{Fe}(\text{NO})_2]^{2-}$	7113.3	14
$[(\text{OC}_7\text{H}_4\text{SN}-)_2\text{Fe}(\text{NO})_2]^{2-}$	7113.2	14
$[(\text{PPh}_3)_2\text{Fe}(\text{NO})_2]$	7113.7	10
$\{\text{Fe}(\text{NO})_2\}_2^9$		
$[(\text{NO})_2\text{Fe}(\text{SET})_2]^-$	7113.6	8e
$[(\text{NO})_2\text{Fe}(\text{OPh})_2]^-$	7113.7	3e
$[(-\text{SC}_7\text{H}_4\text{SN})_2\text{Fe}(\text{NO})_2]^-$	7113.7	8b
$[(\text{OC}_7\text{H}_4\text{SN}-)_2\text{Fe}(\text{NO})_2]^-$	7113.6	14

$\{\text{Fe}^{\text{III}}(\text{NO}^-)_2\}_2^9$,^{3e,12b} the electronic structure of the $\{\text{Fe}(\text{NO})_2\}_2^{10}\{\text{Fe}(\text{NO})_2\}_2^{10}$ core of the dinuclear complex 1 may be assigned as $\{\text{Fe}^{\text{II}}(\text{NO}^-)_2\}_2^{10}\{\text{Fe}^{\text{II}}(\text{NO}^-)_2\}_2^{10}$.

It is of importance to note that the preedge energy was known to correlate with the metal oxidation state under the presence of the same coordination geometries and ligand types.²⁰ Taking the apparent peak position of the preedge for comparison, complex 2 displaying the lower preedge energy 7113.2 eV, compared to those of the $\{\text{Fe}(\text{NO})_2\}_2^{10}\{\text{Fe}(\text{NO})_2\}_2^9$ **rRRE-S^tBu** (7113.4 eV) and the $\{\text{Fe}(\text{NO})_2\}_2^9\{\text{Fe}(\text{NO})_2\}_2^9$ $[(\text{NO})_2\text{Fe}(\mu\text{-S}^t\text{Bu})_2]$ (7113.8 eV) (Figure 5),^{3e} may implicate the lower oxidation state of Fe in complex 2. Because the

dominant $\{\text{Fe}^{\text{III}}(\text{NO}^-)_2\}_2^9\{\text{Fe}^{\text{III}}(\text{NO}^-)_2\}_2^9$ electronic structure of complex $[(\text{NO})_2\text{Fe}(\mu\text{-S}^t\text{Bu})_2]$ was concluded on the basis of the Fe K-edge preedge energy and the relative d-manifold energy derived from S K-edge XAS,^{3e,21} the electronic structure of the $\{\text{Fe}(\text{NO})_2\}_2^{10}\{\text{Fe}(\text{NO})_2\}_2^{10}$ core of complex 2 is best described as $\{\text{Fe}^{\text{II}}(\text{NO}^-)_2\}_2^{10}\{\text{Fe}^{\text{II}}(\text{NO}^-)_2\}_2^{10}$.

Taking the peak position of the K-edge preedge for comparison (Table 2), the energy shifts from 7113.6 eV ($\{\text{Fe}(\text{NO})_2\}_2^9$ $[(\text{NO})_2\text{Fe}(\text{SET})_2]^-$) to 7113.2 eV ($\{\text{Fe}(\text{NO})_2\}_2^{10}$ $[(\text{NO})_2\text{Fe}(\text{SET})_2]^{2-}$) upon one-electron reduction of $\{\text{Fe}(\text{NO})_2\}_2^9$ $[(\text{NO})_2\text{Fe}(\text{SET})_2]^-$ (Figure 6). As shown in Figures S2–S4 in the SI, the strong π -acceptor PPh_3 -coordinated $\{\text{Fe}(\text{NO})_2\}_2^{10}$ core of the $\{\text{Fe}(\text{NO})_2\}_2^{10}$ DNIC $[(\text{NO})_2\text{Fe}(\text{PPh}_3)_2]$ increasing the Z_{eff} of the Fe center may rationalize the higher Fe K-edge preedge energy (7113.7 eV), compared to those of the $\{\text{Fe}(\text{NO})_2\}_2^{10}$ DNIC $[(\text{NO})_2\text{Fe}(\text{sparteine})]$ (7113.2 eV), $[(\text{NO})_2\text{Fe}(\text{TMEDA})]$ (7113.1 eV), and complex 3 (7113.2 eV). This result demonstrates that Fe K-edge absorption of DNICs is strongly perturbed by the ligand environment, in addition to the metal oxidation state and coordination geometry. Compared to the preedge energy derived from the $\text{Fe}_{1s} \rightarrow \text{Fe}_{3d}$ transition falling within the range of 7113.6–7113.8 eV for the dinuclear $\{\text{Fe}(\text{NO})_2\}_2^9\{\text{Fe}(\text{NO})_2\}_2^9$ DNICs²¹ and 7113.4–7113.8 eV for the mononuclear $\{\text{Fe}(\text{NO})_2\}_2^9$ DNICs (Table 2),^{3e} we conclude that the $\{\text{Fe}(\text{NO})_2\}_2^{10}$ mononuclear DNICs and the $\{\text{Fe}(\text{NO})_2\}_2^{10}\{\text{Fe}(\text{NO})_2\}_2^{10}$ dinuclear DNICs containing S/O/N-ligation modes display the characteristic preedge energy falling in the range of 7113.1–7113.3 eV, which may be adopted to probe the formation of the EPR-silent dinuclear $\{\text{Fe}(\text{NO})_2\}_2^{10}\{\text{Fe}(\text{NO})_2\}_2^{10}$ DNICs and mononuclear $\{\text{Fe}(\text{NO})_2\}_2^{10}$ DNICs in biology.

The S K-edge spectra of complexes $[(\text{NO})_2\text{Fe}(\mu\text{-S}^t\text{Bu})_2]$, **rRRE-S^tBu**, and 2 are depicted in Figure 7. The corresponding

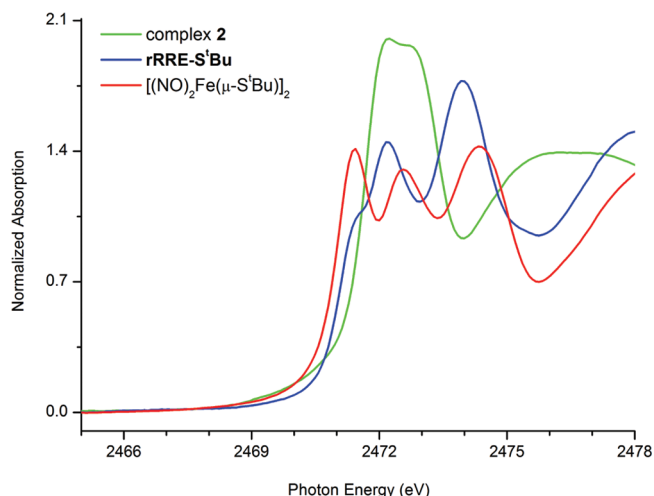


Figure 7. S K-edge spectra of complexes $[(\text{NO})_2\text{Fe}(\mu\text{-S}^t\text{Bu})_2]$, **rRRE-S^tBu**, and 2.

preedge transitions and thiolate peaks are listed in Table S1 in the SI. The decrease of the transition energy of $\text{S}_{1s} \rightarrow \text{S}_{c-s} \sigma^*$ from 2474.5 eV ($[(\text{NO})_2\text{Fe}(\mu\text{-S}^t\text{Bu})_2]$) to 2473.8 eV (**rRRE-S^tBu**) to 2473.0 eV (complex 2) indicates the decreasing effective nuclear charge of sulfur from the bridging thiolates of $\{\text{Fe}(\text{NO})_2\}_2^9\{\text{Fe}(\text{NO})_2\}_2^9$ $[(\text{NO})_2\text{Fe}(\mu\text{-S}^t\text{Bu})_2]$ to the bridging thiolates of complex 2. This is consistent with the trend of the

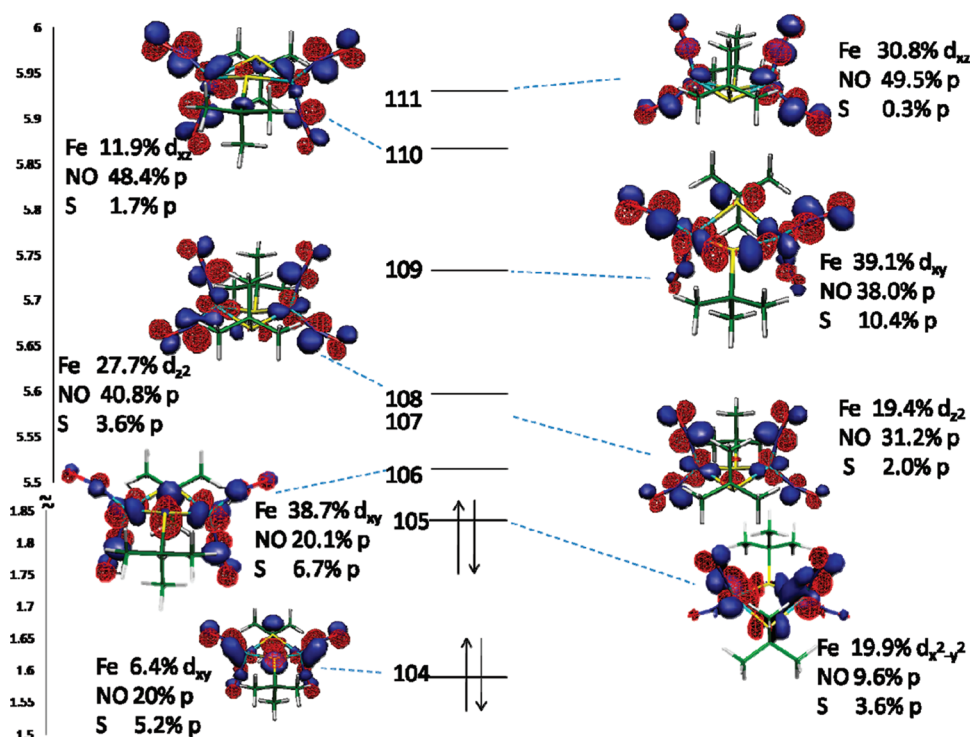


Figure 8. MO diagram of complex 2. Numbers shown are the percentage of Fe 3d, NO 2p, and S 3p orbitals in each MO.

Mulliken average charge population on S atoms with +0.072, −0.065, and −0.09 in $[(\text{NO})_2\text{Fe}(\mu\text{-S}^t\text{Bu})]_2$, **rRRE-S^tBu**, and **2**, respectively. The relative d-manifold energy shift is estimated by setting the reference energy levels on complex **2**. The estimated method is based on the serial publications in Solomon's group.²² According to the results listed in Table S1 in the SI, the relative d-manifold energy decreases from complex **2** to **rRRE-S^tBu** to $[(\text{NO})_2\text{Fe}(\mu\text{-S}^t\text{Bu})]_2$ by 0.8 and 1.4 eV, respectively. This implies that one-electron oxidation may increase the effective nuclear charge (Z_{eff}) of Fe to induce an increase of about 0.7–0.8 eV shift, so that the observed apparent preedge peak of Fe K-edge displays an increase from 7113.2 to 7113.4 to 7113.8 eV upon going from complex **2** to **rRRE-S^tBu** to $[(\text{NO})_2\text{Fe}(\mu\text{-S}^t\text{Bu})]_2$, respectively.

Molecular Orbital (MO) and Time-Dependent DFT (TD-DFT) Calculations. The MO diagram of complex **2** is depicted in Figure 8, and those of $[(\text{NO})_2\text{Fe}(\mu\text{-S}^t\text{Bu})]_2$ and **rRRE-S^tBu** are shown in Figures S5 and S6 in the SI, respectively. In comparison with MO diagrams of $[(\text{NO})_2\text{Fe}(\mu\text{-SEt})]_2$ ($z = 0, 1-$),^{16b,21} the LUMO (MO 105) of $[(\text{NO})_2\text{Fe}(\mu\text{-S}^t\text{Bu})]_2$ and **rRRE-S^tBu**, respectively, was mainly the antibonding character between Fe $3d_{x^2-y^2}$ and S atoms. This rationalized the increase of the Fe–S bond lengths via the consecutive reduction $[(\text{NO})_2\text{Fe}(\mu\text{-S}^t\text{Bu})]_2 \rightarrow \text{rRRE-S}^t\text{Bu} \rightarrow \text{2}$ (Table 1).

The S K-edge spectrum of $[(\text{NO})_2\text{Fe}(\mu\text{-S}^t\text{Bu})]_2$ showed two well-resolved preedge absorption peaks at 2471.4 and 2472.5 eV. Upon one-electron reduction of $[(\text{NO})_2\text{Fe}(\mu\text{-S}^t\text{Bu})]_2$ yielding **rRRE-S^tBu**, the absorption peaks shift to 2471.4 eV (shoulder) and 2472.2 eV. Interestingly, only one preedge absorption peak at 2472.0 eV was observed in complex **2**. The TD-DFT calculation of these S K-edge preedge transitions and its comparison with experimental results are displayed in Figures 9 and S7 and S8 in the SI for complexes **2**, $[(\text{NO})_2\text{Fe}(\mu\text{-S}^t\text{Bu})]_2$, and **rRRE-S^tBu**, respectively. On the

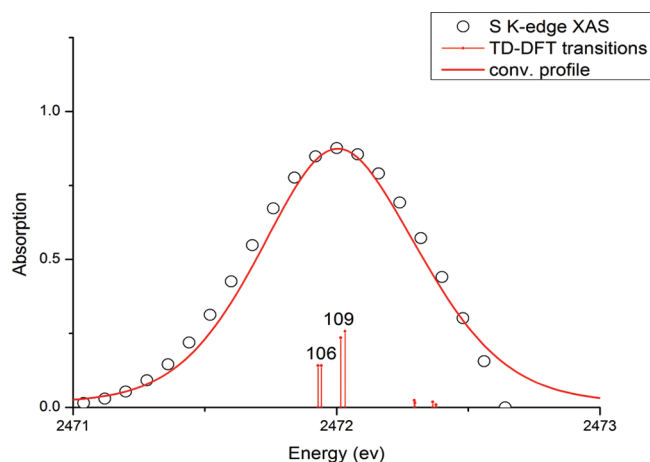


Figure 9. Experimental (O) and TD-DFT-calculated (red solid line) preedge absorption of complex **2**. The theoretically calculated transition peaks are displayed in the vertical lines. All transitions have been convolved with a pseudo-Voigt function with a 1:1 ratio of Lorentzian to Gaussian and of 0.3 eV half-width to account for experiment and core-hole broadening. The transition energy is shifted by 40.6 eV to gain better agreement between the experimental and calculated profiles.

basis of the TD-DFT results, the peak observed at 2471.4 eV for $[(\text{NO})_2\text{Fe}(\mu\text{-S}^t\text{Bu})]_2$ and **rRRE-S^tBu**, respectively, is corresponding to the transition of S 1s to the LUMO dominated by the contributions with Fe $3d_{x^2-y^2}$ and S 3p (MO 105/105 β shown in Figures S5 and S6 in the SI). The second absorption peak at 2472.5 eV for complex $[(\text{NO})_2\text{Fe}(\mu\text{-S}^t\text{Bu})]_2$ (2472.2 eV for **rRRE-S^tBu**) was attributed to the transitions from S 1s to unoccupied MOs related to Fe–S antibonding and to the antibonding orbital mainly contributed from S, NO π^* , and Fe 3d orbitals (MO 106–109 shown in Figures 8 and S5 and S6 in the SI).

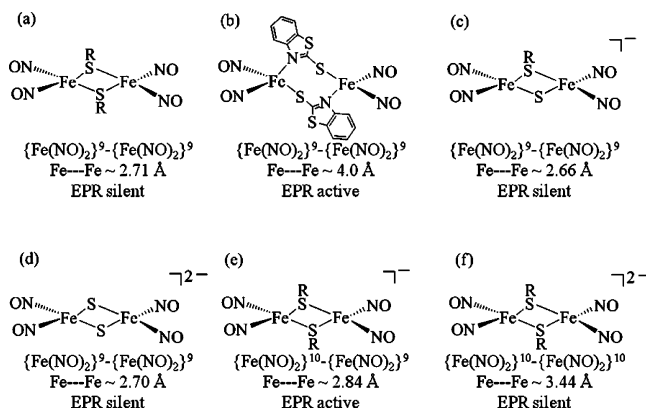
On the basis of the MO diagram of the mononuclear $\{\text{Fe}(\text{NO})_2\}^9$ $[(\text{NO})_2\text{Fe}(\text{SEt})_2]^-$ reported in the previous study,²¹ the MO 61β ($\sim 55.2\%$ Fe d_{2z} , $\sim 8.7\%$ NO, and $\sim 12.2\%$ S) acts as the electron-acceptor orbital for the one-electron reduction of the mononuclear $\{\text{Fe}(\text{NO})_2\}^9$ $[(\text{NO})_2\text{Fe}(\text{SEt})_2]^-$, yielding the $\{\text{Fe}(\text{NO})_2\}^{10}$ DNIC **3** (Figure S9 in the SI). Reduction of $\{\text{Fe}^{\text{III}}(\text{NO}^-)_2\}^9$ yielding $\{\text{Fe}^{\text{II}}(\text{NO}^-)_2\}^{10}$ and the only one preedge absorption peak observed in the S K-edge spectrum of complex **3** are related to the Fe–S σ^* antibonding orbitals (Figures S10 and S11 in the SI).

CONCLUSION AND COMMENTS

Studies on the syntheses of the $\{\text{Fe}(\text{NO})_2\}^{10}$ DNIC **3** and the $\{\text{Fe}(\text{NO})_2\}^9\{\text{Fe}(\text{NO})_2\}^{10}$ complexes **1** and **2** have resulted in the following results:

- (1) The $\{\text{Fe}(\text{NO})_2\}^9$ DNIC $[(\text{NO})_2\text{Fe}(\text{SEt})_2]^-$, $\{\text{Fe}(\text{NO})_2\}^9\{\text{Fe}(\text{NO})_2\}^9$ $[(\text{NO})_2\text{Fe}(\mu\text{-S}^t\text{Bu})_2]$, the delocalized $\{\text{Fe}(\text{NO})_2\}^{10}\{\text{Fe}(\text{NO})_2\}^9$ **rRRE-S^tBu**, and the $\{\text{Fe}(\text{NO})_2\}^{10}\{\text{Fe}(\text{NO})_2\}^{10}$ complex **2** are chemically interconvertible. The reversible redox processes of $\mathbf{2} \rightleftharpoons \mathbf{rRRE-S}^t\text{Bu} \rightleftharpoons [(\text{NO})_2\text{Fe}(\mu\text{-S}^t\text{Bu})_2]$ are presumed to mainly occur at the redox-active Fe centers. The different oxidation levels of the $\{\text{Fe}(\text{NO})_2\}\{\text{Fe}(\text{NO})_2\}$ units for complexes $[(\text{NO})_2\text{Fe}(\mu\text{-S}^t\text{Bu})_2]$, **rRRE-S^tBu**, and **2** reflect the distinctly different Fe...Fe distance [2.705(1) Å for $[(\text{NO})_2\text{Fe}(\mu\text{-S}^t\text{Bu})_2]$, 2.958(1) Å for **rRRE-S^tBu**, and 3.437(1) Å for complex **2**] to reach the optimum electron density surrounding the $\{\text{Fe}(\text{NO})_2\}\{\text{Fe}(\text{NO})_2\}$ core. The detailed spectroscopic analysis (IR ν_{NO} spectra and Fe/S K-edge preedge energy) may provide a superior level of insight into the discrimination of $[(\text{NO})_2\text{Fe}(\mu\text{-S}^t\text{Bu})_2]$ [IR ν_{NO} 1809 vw, 1778 s, 1753 s cm^{-1} (KBr)], **rRRE-S^tBu** [IR ν_{NO} 1674 s, 1651 s cm^{-1} (KBr)], and complex **2** [IR ν_{NO} 1637 m, 1613 s, 1578 s, 1567 s cm^{-1} (KBr)]. According to the absence of the EPR signal and the lower Fe K-edge preedge energy 7113.2 eV (vs 7113.4 and 7113.8 eV for **rRRE-S^tBu** and $[(\text{NO})_2\text{Fe}(\mu\text{-S}^t\text{Bu})_2]$, respectively),^{3e,12b} the electronic structure of the $\{\text{Fe}(\text{NO})_2\}^{10}\{\text{Fe}(\text{NO})_2\}^{10}$ core of complex **2** is best described as $\{\text{Fe}^{\text{II}}(\text{NO}^-)_2\}^{10}$ - $\{\text{Fe}^{\text{II}}(\text{NO}^-)_2\}^{10}$.^{3e,12b,21}
- (2) This study, including certain results from earlier studies,^{3e} demonstrates that the binding affinity of ligands ($[\text{SR}]^-$ (R = alkyl) and $[\text{OPh}]^-$) toward $\{\text{Fe}(\text{NO})_2\}^9$ and $\{\text{Fe}(\text{NO})_2\}^9\{\text{Fe}(\text{NO})_2\}^9$ motifs, respectively, is in the order of $[\text{SR}]^- > [\text{OPh}]^-$. It may rationalize that most of the DNICs and RREs characterized and proposed nowadays are bound to protein through cysteinate side chains in biology.^{1f,4}
- (3) As indicated in Chart 1, the dinuclear DNICs can be classified according to oxidation levels and configurations: (a) the EPR-silent neutral $\{\text{Fe}(\text{NO})_2\}^9\{\text{Fe}(\text{NO})_2\}^9$ RRE,¹⁵ (b) the EPR-active neutral $\{\text{Fe}(\text{NO})_2\}^9\{\text{Fe}(\text{NO})_2\}^9$ RRE containing two separate $\{\text{Fe}(\text{NO})_2\}^9$ motifs,^{7a} (c) the EPR-silent anionic $\{\text{Fe}(\text{NO})_2\}^9\{\text{Fe}(\text{NO})_2\}^9$ RRE containing mixed thiolate-sulfide-bridged ligands,²³ (d) the EPR-silent $\{\text{Fe}(\text{NO})_2\}^9\{\text{Fe}(\text{NO})_2\}^9$ Roussin's red salt,²⁴ (e) the EPR-active $\{\text{Fe}(\text{NO})_2\}^9\{\text{Fe}(\text{NO})_2\}^9$ reduced RREs,¹⁶ and (f) the EPR-silent $\{\text{Fe}(\text{NO})_2\}^{10}\{\text{Fe}(\text{NO})_2\}^{10}$ dianionic reduced RREs.

Chart 1



- (4) The $\{\text{Fe}(\text{NO})_2\}^{10}$ DNIC **3** and the $\{\text{Fe}(\text{NO})_2\}^9$ DNIC $[\text{K-18-crown-6 ether}][(\text{NO})_2\text{Fe}(\text{SEt})_2]$ are chemically interconvertible without decomposition. On the basis of IR ν_{NO} stretching frequencies, Fe–N (N–O) bond distances and Fe K-edge preedge energy of DNIC **3**, the electronic structure of $\{\text{Fe}(\text{NO})_2\}^{10}$ core of DNIC **3** is best described as $\{\text{Fe}^{\text{II}}(\text{NO}^-)_2\}^{10}$. Instead of the formation of the dinuclear EPR-silent $\{\text{Fe}(\text{NO})_2\}^{10}\{\text{Fe}(\text{NO})_2\}^{10}$ **2**, reduction of the $\{\text{Fe}(\text{NO})_2\}^9$ DNIC $[\text{K-18-crown-6 ether}][(\text{NO})_2\text{Fe}(\text{SEt})_2]$ by KC_8 + $[\text{18-crown-6 ether}]$ affording the thermally stable dianionic reduced monomeric $\{\text{Fe}(\text{NO})_2\}^{10}$ DNIC **3** demonstrates that the site-selective $[\text{Fe}(\text{SR})_2 \cdots (\text{K}^+)_2]$ interactions play a crucial role in regulating the formation of the $\{\text{Fe}(\text{NO})_2\}^{10}\{\text{Fe}(\text{NO})_2\}^{10}$ **2** or the mononuclear $\{\text{Fe}(\text{NO})_2\}^{10}$ **3** upon reduction of the $\{\text{Fe}(\text{NO})_2\}^9$ DNICs $[(\text{NO})_2\text{Fe}(\text{SR})_2]$ (cation = K^+ -18-crown-6 ether, PPN^+).
- (5) Compared to the Fe K-edge preedge energy falling within the range of 7113.6–7113.8 eV for the dinuclear $\{\text{Fe}(\text{NO})_2\}^9\{\text{Fe}(\text{NO})_2\}^9$ DNICs and 7113.4–7113.8 eV for the mononuclear $\{\text{Fe}(\text{NO})_2\}^9$ DNICs,^{3e,21} the $\{\text{Fe}(\text{NO})_2\}^{10}$ dianionic reduced monomeric DNICs and the $\{\text{Fe}(\text{NO})_2\}^{10}\{\text{Fe}(\text{NO})_2\}^{10}$ dianionic reduced RREs containing S/O/N-ligation modes display the characteristic preedge energy falling in the range of 7113.1–7113.3 eV (Table 2). Also, the distinct S K-edge preedge absorption energy and pattern can serve as an efficient tool to unambiguously characterize and discriminate the various oxidation-state dinuclear $\{\text{Fe}(\text{NO})_2\}^9\{\text{Fe}(\text{NO})_2\}^9$ DNICs.

These results provide some clues to signify that protein-bound $\{\text{Fe}(\text{NO})_2\}^{10}$ DNICs stabilized by the intermolecular $[\text{Fe}(\text{SR})_2 \cdots (\text{K}^+)_2]$ interactions and $\{\text{Fe}(\text{NO})_2\}^{10}\{\text{Fe}(\text{NO})_2\}^{10}$ dianionic reduced RREs may exist in biology. Also, this biomimetic study may lend support to the proposal that the cysteine-containing $\{\text{Fe}(\text{NO})_2\}^{10}$ DNICs, $\{\text{Fe}(\text{NO})_2\}^{10}\{\text{Fe}(\text{NO})_2\}^{10}$ RREs, and $\{\text{Fe}(\text{NO})_2\}^{10}\{\text{Fe}(\text{NO})_2\}^9$ reduced RREs may be regarded as the potential species derived from nitrosylation of $[\text{Fe-S}]$ proteins in biology. In particular, the existence (function) for the diversity of DNICs/RREs, i.e., $\{\text{Fe}(\text{NO})_2\}^{10}$ DNICs and $\{\text{Fe}(\text{NO})_2\}^{10}\{\text{Fe}(\text{NO})_2\}^{10}$ RREs, may be shrouded in biological evolution and most likely include bioavailability of a given DNICs/RREs during repair of the modified $[\text{Fe-S}]$ proteins.

EXPERIMENTAL SECTION

Manipulations, reactions, and transfers were conducted under nitrogen according to Schlenk techniques or in a glovebox (N_2 gas). Solvents were distilled under nitrogen from appropriate drying agents (diethyl ether from CaH_2 ; acetonitrile from $CaH_2-P_2O_5$; hexane and THF from sodium benzophenone) and stored in dried, N_2 -filled flasks over 4 Å molecular sieves. Nitrogen was purged through these solvents [including dimethylformamide (DMF)] before use. Solvent was transferred to the reaction vessel via a stainless steel cannula under positive pressure of N_2 . The reagents potassium hydroxide (Aldrich), phenol (TCI), bis(triphenylphosphoranylidene)ammonium chloride ([PPN][Cl], Fluka), graphite (Alfa Aesar), potassium (High Purity Chemical), 18-crown-6 ether (TCI), 2-methyl-2-propanthiol (Aldrich), ethylthiol (Aldrich), and ferrocenium tetrafluoroborate ($[Cp_2Fe][BF_4]$, Aldrich) were used as received. Complexes $[(NO)_2Fe(OPh)_2]^-$, $[(NO)_2Fe(SET)_2]^-$, $[(NO)_2Fe(S^tBu)_2]^-$, $[Fe(\mu-S^tBu)(NO)_2]_2$, $[Fe(\mu-S^tBu)(NO)_2]_2^-$, $[(-SC_7H_4SN)_2Fe(NO)_2]^-$, $[(-SC_7H_4SN)_2Fe(NO)_2]^{2-}$, $[(OC_7H_4SN)_2Fe(NO)_2]^-$, $[(OC_7H_4SN)_2Fe(NO)_2]^{2-}$, $[(sparteine)Fe(NO)_2]$, $[(TMEDA)Fe(NO)_2]$, and $[PPh_3]_2Fe(NO)_2$ were synthesized on the basis of the literature reported.^{3e,8,10,14,16} IR spectra of the ν_{NO} stretching frequencies were recorded on a PerkinElmer model Spectrum One B spectrometer with sealed solution cells (0.1 mm, KBr or CaF_2 windows) or a KBr solid. UV-vis spectra were recorded on a Jasco V-570 spectrometer. Electrochemical measurements were performed with a CHI model 421 potentiostat (CH Instrument) instrumentation. Cyclic voltammograms were obtained from 2.5 mM analyte concentration in O_2 -free CH_3CN using 0.1 M $[nBu_4N][PF_6]$ as the supporting electrolyte. The potential was measured at 298 K vs a Ag/AgCl reference electrode by using a glassy carbon working electrode. Analyses of carbon, hydrogen, and nitrogen were obtained with a CHN analyzer (Heraeus).

Reaction of $[PPN][(NO)_2Fe(OPh)_2]$ and KC_8 Affording 1. The THF solution of complex $[PPN][(NO)_2Fe(OPh)_2]$ (0.168 g, 0.2 mmol) and $[PPN][Cl]$ (0.115 g, 0.2 mmol) was transferred via a cannula under positive N_2 to a Schlenk tube loaded with KC_8 (0.030 g, 0.22 mmol). The mixture solution was stirred for 10 min at 0 °C and then dried under vacuum. The crude green solid was redissolved in DMF- CH_3CN , and then the solution was filtered through Celite to remove the insoluble graphite. The addition of diethyl ether to the filtrate led to precipitation of green solid 1 (yield 0.092 g, 61%). Diffusion of diethyl ether into the DMF- CH_3CN solution of complex 1 at -20 °C led to dark-green crystals suitable for single-crystal X-ray diffraction. IR ν_{NO} : 1651 s, 1602 s cm^{-1} (CH_3CN), 1651 s, 1600 s cm^{-1} (KBr). Absorption spectrum (CH_3CN) [λ_{max} nm (ϵ , $M^{-1} cm^{-1}$): 272 (8949), 310 (8465), 381 (2280), 854 (586)]. Anal. Calcd for $C_{84}H_{70}Fe_2N_6O_4P_4 \cdot CH_3CN$: C, 67.24; H, 4.79; N, 6.38. Found: C, 66.80; H, 5.13; N, 6.55.

Reaction of 1, $[Cp_2Fe][BF_4]$, and $[K][OPh]$ Yielding $[PPN]-(NO)_2Fe(OPh)_2$. Complex 1 (0.149 g, 0.1 mmol) and $[Cp_2Fe][BF_4]$ (0.054 g, 0.2 mmol) were dissolved in CH_3CN (10 mL) and stirred for 5 min at 0 °C. The resulting solution was transferred into the flask containing $[K][OPh]$ (0.026 g, 0.2 mmol) and 18-crown-6 ether (0.053 g, 0.2 mmol) by a cannula under positive N_2 pressure. After being stirred for 5 min, the reaction was monitored by FTIR. The IR spectrum [1746 m, 1680 s cm^{-1} (ν_{NO}) (CH_3CN)] was assigned to the formation of the known complex $[PPN]-(NO)_2Fe(OPh)_2$.^{3e} The red-brown solution was dried under vacuum and redissolved in THF. The red-brown solution was then filtered through Celite to remove the insoluble solid. Hexane was added into the filtrate to precipitate the brown solid $[PPN]-(NO)_2Fe(OPh)_2$ (yield 0.126 g, 75%) characterized by IR and UV-vis spectroscopy.

Reaction of 1 and [K-18-crown-6 ether][S^tBu] Yielding 2. Complex 1 (0.149 g, 0.1 mmol), $[K][S^tBu]$ (0.026 g, 0.2 mmol), and 18-crown-6 ether (0.053 g, 0.2 mmol) were dissolved in CH_3CN (10 mL) and stirred for 30 min at ambient temperature. Diethyl ether (3 mL) was added to the resulting solution and stirred for 10 min. The mixture solution was then filtered through Celite to remove the insoluble solid. Additional diethyl ether (15 mL) was added to the

filtrate to lead to the precipitation of green solid 2 (yield 0.125 g, 83%). Diffusion of diethyl ether into the CH_3CN solution of complex 2 at -20 °C led to dark-green crystals suitable for single-crystal X-ray diffraction. IR ν_{NO} : 1637 m, 1613 s, 1578 s, 1567 s cm^{-1} (KBr); 1641 m, 1616 s, 1578 vs, 1563 sh cm^{-1} (DMSO). Absorption spectrum (CH_3CN) [λ_{max} nm (ϵ , $M^{-1} cm^{-1}$): 270 (8454), 396 (2013)]. Anal. Calcd for $C_{80}H_{78}Fe_2N_6O_4P_4S_2 \cdot CH_3CN$: C, 64.44; H, 5.34; N, 6.42. Found: C, 64.29; H, 5.48; N, 6.42.

Reaction of $[PPN]-(NO)_2Fe(S^tBu)_2$ and 1 equiv of KC_8 Yielding 2. The THF solution of complex $[PPN]-(NO)_2Fe(S^tBu)_2$ (0.166 g, 0.2 mmol) and $[PPN][Cl]$ (0.115 g, 0.2 mmol) was transferred via a cannula under positive N_2 to a Schlenk tube loaded with KC_8 (0.030 g, 0.22 mmol). The mixture solution was stirred for 10 min at 0 °C and then dried under vacuum. The crude green solid was redissolved in CH_3CN , and then the solution was filtered through Celite to remove the insoluble graphite under a N_2 atmosphere. The addition of diethyl ether to the filtrate led to the precipitation of green solid 2 (yield 0.108 g, 73%) characterized by IR and UV-vis spectroscopy.

Reaction of $[PPN]-(NO)_2Fe(S^tBu)_2$ and 0.5 equiv of KC_8 Affording $[PPN][Fe(\mu-S^tBu)(NO)_2]_2$ (rRRE-S^tBu). The THF solution of complex $[PPN]-(NO)_2Fe(S^tBu)_2$ (0.166 g, 0.2 mmol) and $[PPN][Cl]$ (0.057 g, 0.1 mmol) was transferred via a cannula under positive N_2 to a Schlenk tube loaded with KC_8 (0.015 g, 0.11 mmol). After being stirred for 10 min at 0 °C, the reaction was monitored by FTIR. The IR spectrum [1672 s, 1654 s cm^{-1} (ν_{NO}) (THF)] was assigned to the formation of the known complex $[PPN][Fe(\mu-S^tBu)(NO)_2]_2$ (rRRE-S^tBu).¹⁶ The dark-green solution was then filtered through Celite to remove the insoluble solid under a N_2 atmosphere. Hexane was added into the filtrate to precipitate the green solid rRRE-S^tBu (yield 0.083 g, 87%) characterized by IR and UV-vis spectroscopy.

Reaction of $[PPN][Fe(\mu-S^tBu)(NO)_2]_2$ (rRRE-S^tBu) and KC_8 Yielding 2. The THF solution of complex $[PPN][Fe(\mu-S^tBu)(NO)_2]_2$ (0.095 g, 0.1 mmol) and $[PPN][Cl]$ (0.057 g, 0.1 mmol) was transferred via a cannula under positive N_2 to a Schlenk tube loaded with KC_8 (0.015 g, 0.11 mmol). The mixture solution was stirred for 10 min at 0 °C and then dried under vacuum. The crude green solid was redissolved in CH_3CN , and then the solution was filtered through Celite to remove the insoluble graphite under a N_2 atmosphere. The addition of diethyl ether to the filtrate led to the precipitation of green solid 2 (yield 0.117 g, 79%) characterized by IR and UV-vis spectroscopy.

Reaction of [K-18-crown-6 ether] $[(NO)_2Fe(SET)_2]$ and 1 equiv of $[KC_8]$ + [18-crown-6 ether] Affording 3. The THF solution of complex [K-18-crown-6 ether] $[(NO)_2Fe(SET)_2]$ (0.108 g, 0.2 mmol) and 18-crown-6 ether (0.053 g, 0.2 mmol) was transferred via a cannula under positive N_2 to a Schlenk tube loaded with KC_8 (0.030 g, 0.22 mmol). The mixture solution was stirred for 10 min at 0 °C and then monitored by FTIR [1614 m, 1571 s cm^{-1} (ν_{NO}) (THF)]. The resulting solution was then filtered through Celite to remove the insoluble graphite under a N_2 atmosphere. The addition of hexane to the filtrate led to the precipitation of green solid 3 (yield 0.070 g, 41%). Diffusion of hexane into the THF solution of complex 3 at room temperature led to dark-green crystals suitable for single-crystal X-ray diffraction. IR ν_{NO} : 1614 m, 1571 s cm^{-1} (THF), 1604 s, 1560 s cm^{-1} (KBr). Absorption spectrum (THF) [λ_{max} nm (ϵ , $M^{-1} cm^{-1}$): 370 (1128), 423 (770)]. Anal. Calcd for $C_{28}H_{58}FeK_2N_2O_{14}S_2$: C, 39.80; H, 6.92; N, 3.32. Found: C, 40.03; H, 7.00; N, 3.50.

XAS Measurements. All XAS experiments were carried out at NSRRC, Hsinchu, Taiwan. Both Fe and S K-edge spectra were recorded at room temperature. The spectra were reduced and normalized based on the procedures reported by Solomon and co-workers.²⁵ Data were averaged, and a smooth background was removed from all spectra by fitting a straight line to the preedge region and subtracting this straight line from the entire spectrum. Normalization of the data was accomplished by fitting a flat polynomial to the postregion and normalizing the edge jump to 1.0 at 7400 eV for Fe K-edge spectra and 2550 eV for S K-edge spectra. For Fe K-edge measurements, experiments were performed in

transmission mode at the BL17C wiggler beamline with a double-crystal Si(111) monochromator. The energy resolution $\Delta E/E$ was estimated to be about 2×10^{-4} . High harmonics were rejected by Rh-coated mirrors. The spectra were scanned from 6.912 to 8.006 keV. A reference Fe foil is always measured simultaneously, in which the first inflection point at 7112.0 eV of the Fe foil spectrum is used for energy calibration. Ion chambers used to measure the incident (I_0) and transmitted (I) beam intensities were filled with a mixture of N_2 and He gases and a mixture of N_2 and Ar gases, respectively.

The S K-edge data were collected in fluorescence mode at BL 16A with a Si(111) monochromator. The energy resolution $\Delta E/E$ is 1.4×10^{-4} . The energy is scanned from 2.42 to 2.77 keV. A Lytle detector was employed for fluorescence measurements in which the sample chamber is filled with high-purity He gas to avoid air absorption. Samples were ground to powder from single crystals and secured in the bag made of 3.6 μm Mylar film. The absorption of the S K-edge region of the empty bag made of 3.6 μm Mylar film was verified to be negligible. The photon energy was calibrated to the maximum of the first pre-edge feature of $\text{Na}_2\text{S}_2\text{O}_3 \cdot 5\text{H}_2\text{O}$ at 2472.02 eV.²⁵ The uncertainty in pre-edge and edge energies is limited by the reproducibility of the edge spectra (~ 0.35 eV for Fe K-edge and ~ 0.1 eV for S K-edge). Thus, the relative energies of the features are reported with errors of ± 0.35 eV for Fe K-edge and ± 0.1 eV for S K-edge.

MO Calculation. All MO and TD-DFT calculations for S K-edge regions were performed on the ORCA package, version 2.8.0.²⁶ The coordinates used for geometry optimization of complexes $[(\text{NO})_2\text{Fe}(\mu\text{-S}^i\text{Bu})_2]$, **rRRE-SⁱBu**, **2**, and **3** were based on the experimental structures taken from the X-ray diffraction experiments.^{15b,16a} The coordinate system employed is such that the origin is set as the center between two Fe atoms; the x axis is collinear with the Fe1–Fe2 direction; the y axis is perpendicular to the x axis and in the direction of the center to S1. The BP86 functional with the def2-TZVP(f) basis set on the Fe, S, N, O, C, and H atoms was used in the geometry optimization. Complexes $[(\text{NO})_2\text{Fe}(\mu\text{-S}^i\text{Bu})_2]$, **2**, and **3** were calculated at the closed-shell level because of its diamagnetism, but **rRRE-SⁱBu** was done at the unrestricted open-shell level. The optimized coordinates, bond lengths, bond angles, and corresponding experimental crystal data of complexes **2** and **3** are listed in Tables S2 and S4 in the SI. These structures have been checked without imaginary frequency in the ORCA package. The calculated stretching frequencies of NO are also listed in Tables S3 and S5 in the SI. The MO and TD-DFT calculation were done with the B3LYP exchange functional and def2-TZVP(f) basis set. The Löwdin population analysis was used to obtain the contributions of Fe, S, and NO on each MO. Isosurface plots of the MOs were generated using the *Molekel* program, version 4.3, with an isovalue surface at 0.04 au.

Crystallography. Crystallographic data of complexes **1–3** were summarized in Tables S1–S3 in the SI, respectively. The crystals chosen for X-ray diffraction studies measured $0.30 \times 0.30 \times 0.28 \text{ mm}^3$ for complex **1**, $0.18 \times 0.15 \times 0.12 \text{ mm}^3$ for complex **2**, $0.35 \times 0.23 \times 0.06 \text{ mm}^3$ for complex **3**. Each crystal was mounted on a glass fiber and quickly coated in epoxy resin. Unit-cell parameters were obtained by least-squares refinement. Diffraction measurements for complexes **1–3** were carried out on a SMART CCD (Nonius Kappa CCD) diffractometer with graphite-monochromated Mo $K\alpha$ radiation ($\lambda = 0.71073 \text{ \AA}$) and between 1.47 and 28.35° for complex **1**, between 1.15 and 26.41° for complex **2**, and between 1.94 and 25.10° for complex **3**. Least-squares refinement of the positional and anisotropic thermal parameters of all non-H atoms and fixed H atoms was based on F^2 . A SADABS absorption correction was made.²⁷ The SHELXTL structure refinement program was employed.²⁸

■ ASSOCIATED CONTENT

■ Supporting Information

X-ray crystallographic files in CIF format for structure determinations of $[\text{PPN}]_2[\text{Fe}(\mu\text{-OPh})(\text{NO})_2]$, $[\text{PPN}]_2[\text{Fe}(\mu\text{-S}^i\text{Bu})(\text{NO})_2]$, and $[\text{K-18-crown-6 ether}]_2[(\text{NO})_2\text{Fe}(\text{SET})_2]$,

Tables S1–S5, and Figures S1–S11. This material is available free of charge via the Internet at <http://pubs.acs.org>.

■ AUTHOR INFORMATION

Corresponding Author

*E-mail: wfliaw@mx.nthu.edu.tw.

Notes

The authors declare no competing financial interest.

■ ACKNOWLEDGMENTS

We gratefully acknowledge financial support from the National Science Council of Taiwan. Authors thank Pei-Lin Chen and Ting-Shen Kuo for single-crystal X-ray structural determinations. We also thank NSRRC and NCHC for their support on the hardware and software applied in this work.

■ REFERENCES

- (1) (a) Mülsch, A.; Mordvintcev, P. I.; Vanin, A. F.; Busse, R. *FEBS Lett.* **1991**, 294, 252–256. (b) Henry, Y.; Lepoivre, M.; Drapier, J. C.; Ducrocq, C.; Boucher, J. L.; Guissani, A. *FASEB J.* **1993**, 7, 1124–1134. (c) Foster, M. W.; Cowan, J. A. *J. Am. Chem. Soc.* **1999**, 121, 4093–4100. (d) Kennedy, M. C.; Antholine, W. E.; Beinert, H. *J. Biol. Chem.* **1997**, 272, 20340–20347. (e) Toledo, J. C. Jr.; Bosworth, C. A.; Hennon, S. W.; Mahtani, H. A.; Bergonia, H. A.; Lancaster, J. R. Jr. *J. Biol. Chem.* **2008**, 283, 28926–28933. (f) Lewandowska, H.; Meczyńska, S.; Sochanowicz, B.; Sadlo, J.; Kruszewski, M. *J. Biol. Inorg. Chem.* **2007**, 12, 345–352.
- (2) (a) Butler, A. R.; Megson, I. L. *Chem. Rev.* **2002**, 102, 1155–1166. (b) Ueno, T.; Susuki, Y.; Fujii, S.; Vanin, A. F.; Yoshimura, T. *Biochem. Pharmacol.* **2002**, 63, 485–493. (c) Frederik, A. C.; Wiegant, I. Y.; Malyshev, I. Y.; Kleschyov, A. L.; van Faassen, E.; Vanin, A. F. *FEBS Lett.* **1999**, 455, 179–182. (d) McCleverty, J. A. *Chem. Rev.* **2004**, 104, 403–418. (e) Hayton, T. W.; Legzdins, P.; Sharp, W. B. *Chem. Rev.* **2002**, 102, 935–991.
- (3) (a) Szacilowski, K.; Chmura, A.; Stasicka, Z. *Coord. Chem. Rev.* **2005**, 249, 2408–2436. (b) Boese, M.; Keese, M. A.; Becker, K.; Busse, R.; Mülsch, A. *J. Biol. Chem.* **1997**, 272, 21767–21773. (c) Boese, M.; Mordvintcev, P. I.; Vanin, A. F.; Busse, R.; Mülsch, A. *J. Biol. Chem.* **1995**, 270, 29244–29249. (d) Lee, M.; Arosio, P.; Cozzi, A.; Chasteen, N. D. *Biochemistry* **1994**, 33, 3679–3687. (e) Tsai, M.-C.; Tsai, F.-T.; Lu, T.-T.; Tsai, M.-L.; Wei, Y.-C.; Hsu, I.-J.; Lee, J.-F.; Liaw, W.-F. *Inorg. Chem.* **2009**, 48, 9579–9591. (f) Tonzetich, Z. J.; Wang, H.; Mitra, D.; Tinberg, C. E.; Do, L. H.; Jenney, F. E. Jr.; Adams, M. W. W.; Cramer, S. P.; Lippard, S. J. *J. Am. Chem. Soc.* **2010**, 132, 6914–6916.
- (4) Stadler, J.; Bergonia, H. A.; Di Silvio, M.; Sweetland, M. A.; Billiar, T. R.; Simmons, R. L.; Lancaster, J. R. Jr. *Arch. Biochem. Biophys.* **1993**, 302, 4–11.
- (5) Cesareo, E.; Parker, L. J.; Pedersen, J. Z.; Nuccetelli, M.; Mazzetti, A. P.; Pastore, A.; Federici, G.; Caccuri, A. M.; Ricci, G.; Adams, J. J.; Parker, M. W.; Bello, M. L. *J. Biol. Chem.* **2005**, 280, 42172–42180.
- (6) (a) Cruz-Ramos, H.; Crack, J.; Wu, G.; Hughes, N. M.; Scott, C.; Thomson, J. A.; Green, J.; Poole, K. R. *EMBO J.* **2002**, 21, 3235–3244. (b) Kennedy, M. C.; Antholine, E. W.; Beinert, H. *J. Biol. Chem.* **1997**, 272, 20340–20347. (c) Ding, H.; Demple, B. *Proc. Natl. Acad. Sci. U.S.A.* **2000**, 97, 5146–5150.
- (7) (a) Tsai, M.-L.; Hsieh, C.-H.; Liaw, W.-F. *Inorg. Chem.* **2007**, 46, 5110–5117. (b) Tsai, M.-L.; Liaw, W.-F. *Inorg. Chem.* **2006**, 45, 6583–6585.
- (8) (a) Tsai, M.-L.; Chen, C.-C.; Hsu, I.-J.; Ke, S.-C.; Hsieh, C.-H.; Chiang, K.-A.; Lee, G.-H.; Wang, Y.; Liaw, W.-F. *Inorg. Chem.* **2004**, 43, 5159–5167. (b) Tsai, F.-T.; Chiou, S. J.; Tsai, M.-C.; Tsai, M.-L.; Huang, H.-W.; Chiang, M.-H.; Liaw, W.-F. *Inorg. Chem.* **2005**, 44, 5872–5881. (c) Tsai, M.-L.; Liaw, W.-F. *Inorg. Chem.* **2006**, 45, 6583–6585. (d) Hung, M.-C.; Tsai, M.-C.; Lee, G.-H.; Liaw, W.-F. *Inorg. Chem.* **2006**, 45, 6041–6047. (e) Lu, T.-T.; Chiou, S.-J.; Chen, C.-Y.; Liaw, W.-F. *Inorg. Chem.* **2006**, 45, 8799–8806. (f) Chen, T.-N.; Lo,

- F.-C.; Tsai, M.-L.; Shih, K.-N.; Chiang, M.-H.; Lee, G.-H.; Liaw, W.-F. *Inorg. Chim. Acta* **2006**, 359, 2525–2533. (g) Chiou, S.-J.; Wang, C.-C.; Chang, C.-M. *J. Organomet. Chem.* **2008**, 693, 3582–3586. (h) Huang, H.-W.; Tsou, C.-C.; Kuo, T.-S.; Liaw, W.-F. *Inorg. Chem.* **2008**, 47, 2196–2204.
- (9) (a) Hess, J. L.; Hsieh, C.-H.; Reibenspies, J. H.; Darensbourg, M. Y. *Inorg. Chem.* **2011**, 50, 8541–8552. (b) Hsieh, C.-H.; Darensbourg, M. Y. *J. Am. Chem. Soc.* **2010**, 132, 14118–14125. (c) Chiang, C.-Y.; Miller, M. L.; Reibenspies, J. H.; Darensbourg, M. Y. *J. Am. Chem. Soc.* **2004**, 126, 10867–10874. (d) Tonzetich, Z. J.; McQuade, L. E.; Lippard, S. J. *Inorg. Chem.* **2010**, 49, 6338–6348. (e) Baltusis, L. M.; Karlin, K. D.; Rabinowitz, H. N.; Dewan, J. C.; Lippard, S. J. *Inorg. Chem.* **1980**, 19, 2627–2632.
- (10) Albano, V. G.; Araneo, A.; Bellon, P. L.; Chani, G.; Manassero, M. *J. Organomet. Chem.* **1974**, 67, 413–422.
- (11) Reginato, N.; McCrory, C. T. C.; Pervitsky, D.; Li, L. *J. Am. Chem. Soc.* **1999**, 121, 10217–10218.
- (12) (a) Enemark, J. H.; Feltham, R. D. *Coord. Chem. Rev.* **1974**, 13, 339–406. (b) Ye, S.; Neese, F. *J. Am. Chem. Soc.* **2010**, 132, 3646–3647.
- (13) (a) Franz, K. J.; Lippard, S. J. *J. Am. Chem. Soc.* **1998**, 120, 9034–9040. (b) Brown, C. A.; Pavlosky, M. A.; Westre, T. E.; Zhang, Y.; Hedman, B.; Hodgson, K. O.; Solomon, E. I. *J. Am. Chem. Soc.* **1995**, 117, 715–732.
- (14) Wang, J.-H.; Chen, C.-H. *Inorg. Chem.* **2010**, 49, 7644–7646.
- (15) (a) Thomas, J. T.; Robertson, J. H.; Cox, E. G. *Acta Crystallogr.* **1958**, 11, 599–604. (b) Harrop, T. C.; Song, D. T.; Lippard, S. J. *J. Am. Chem. Soc.* **2006**, 128, 3528–3529.
- (16) (a) Tsou, C.-C.; Lu, T.-T.; Liaw, W.-F. *J. Am. Chem. Soc.* **2007**, 129, 12626–12627. (b) Lu, T.-T.; Tsou, C.-C.; Huang, H.-W.; Hsu, I.-J.; Chen, J.-M.; Kuo, T.-S.; Wang, Y.; Liaw, W.-F. *Inorg. Chem.* **2008**, 47, 6040–6050.
- (17) (a) Crayston, A. J.; Glidewell, C.; Lambert, J. R. *Polyhedron* **1990**, 9, 1741–1746. (b) Chau, C.-N.; Wojcicki, A. *Polyhedron* **1992**, 11, 851–852. (c) Glidewell, C. *Polyhedron* **1992**, 11, 2803–2804. (d) Chau, C.-N.; Wojcicki, A. *Polyhedron* **1993**, 12, 1261–1263.
- (18) Wang, R.; Camacho-Fernandez, M. A.; Xu, W.; Zhang, J.; Li, L. *Dalton Trans.* **2009**, 777–786.
- (19) Horrocks, W. D. Jr; Taylor, R. C. *Inorg. Chem.* **1963**, 2, 723–727.
- (20) (a) DuBois, J. L.; Mukherjee, P.; Stack, T. D. P.; Hedman, B.; Solomon, E. I.; Hodgson, K. O. *J. Am. Chem. Soc.* **2000**, 122, 5775–5787. (b) Westre, T. E.; Kennepohl, P.; Dewitt, J. G.; Hedman, B.; Hodgson, K. O.; Solomon, E. I. *J. Am. Chem. Soc.* **1997**, 119, 6297–6314.
- (21) Lu, T.-T.; Lai, S.-H.; Li, Y.-W.; Hsu, I.-J.; Jang, L.-Y.; Lee, J.-F.; Chen, I.-C.; Liaw, W.-F. *Inorg. Chem.* **2011**, 50, 5396–5406.
- (22) (a) Glaser, T.; Rose, K.; Shadle, S. E.; Hedman, B.; Hodgson, K. O.; Solomon, E. I. *J. Am. Chem. Soc.* **2001**, 123, 442–454. (b) Shadle, S. E.; Hedman, B.; Hodgson, K. O.; Solomon, E. I. *Inorg. Chem.* **1994**, 33, 4235–4244. (c) Sun, N.; Liu, L. V.; Dey, A.; Villar-Acevedo, G.; Kovacs, J. A.; Darensbourg, M. Y.; Hodgson, K. O.; Hedman, B.; Solomon, E. *Inorg. Chem.* **2011**, 50, 427–436. (d) Shadle, S. E.; Hedman, B.; Hodgson, K. O.; Solomon, E. I. *J. Am. Chem. Soc.* **1995**, 117, 2259–2272.
- (23) Lu, T.-T.; Huang, H.-W.; Liaw, W.-F. *Inorg. Chem.* **2009**, 48, 9027–9035.
- (24) Sanina, N. A.; Filipenko, O. S.; Aldoshin, S. M.; Ovanesyana, N. *S. Russ. Chem. Bull.* **2000**, 49, 1109–1112.
- (25) (a) Glaser, T.; Hedman, B.; Hodgson, K. O.; Solomon, E. I. *Acc. Chem. Res.* **2000**, 33, 859–868. (b) Solomon, E. I.; Hedman, B.; Hodgson, K. O.; Dey, A.; Szilagyi, R. K. *Coord. Chem. Rev.* **2005**, 249, 97–129. (c) Rose, K.; Shadle, S. E.; Eidsness, M. K.; Kurtz, D. M. Jr.; Scott, R. A.; Hedman, B.; Hodgson, K. O.; Solomon, E. I. *J. Am. Chem. Soc.* **1998**, 120, 10743–10747.
- (26) Neese, F. *ORCA—an ab Initio, Density Functional and Semiempirical Electronic Structure Package*, version 2.8.0; University of Bonn: Bonn, Germany, 2010.
- (27) Sheldrick, G. M. *SADABS*; University of Göttingen: Göttingen, Germany, 1996.
- (28) Sheldrick, G. M. *SHELXTL*; Siemens Analytical X-ray Instruments Inc.: Madison, WI, 1994.